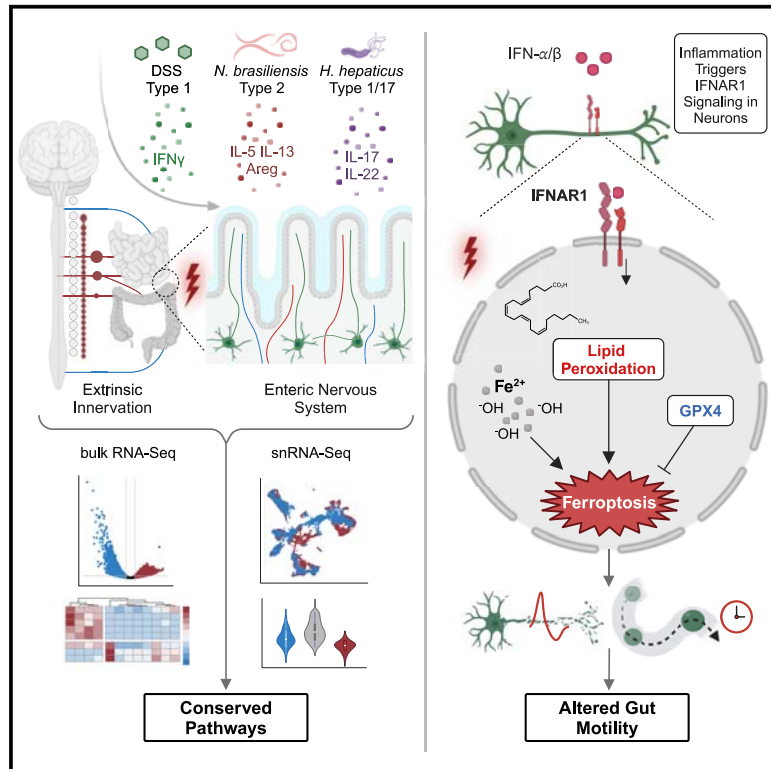# A transcriptional atlas of gut-innervating neurons reveals activation of interferon signaling and ferroptosis during intestinal inflammation

## Graphical abstract



## Authors

Patrycja M. Forster, Manuel O. Jakob, Dilmurat Yusuf, ..., Ahmed N. Hegazy, Jay V. Patankar, Christoph S.N. Klose

## Correspondence

christoph.klose@charite.de

## In brief

Forster, Jakob, et al. perform transcriptional profiling of gut-innervating neurons during intestinal inflammation characterized by a different cytokine milieu. The data reveal a conserved neuronal response to inflammation, including activation of the interferon and ferroptosis pathways.

## Highlights

- Gut-innervating neurons show a conserved response to inflammation

- The interferon signaling pathway is triggered in neurons upon inflammation

- Changes in lipid and arachidonic acid metabolism fuel lipid peroxidation and ferroptosis

- Neuronal *Ifnar1* signaling regulates lipid metabolism, ferroptosis, inflammation, and gut-transit time

**CellPress**

# Neuron

CellPress
OPEN ACCESS

## NeuroResource

# A transcriptional atlas of gut-innervating neurons reveals activation of interferon signaling and ferroptosis during intestinal inflammation

Patrycja M. Forster,[1,12] Manuel O. Jakob,[1,2,12] Dilmurat Yusuf,[3] Marvin Bubeck,[4,5] Heidi Limberger,[4,5] Yanjiang Luo,[6,7] Paula Thieme,[1] Alexandra Polici,[1] Nele Sterczyk,[1] Sotiria Boulekou,[1] Laura Bartel,[1] Catalina Cosovanu,[1] Mario Witkowski,[1,8,9] Miguel González-Acera,[4,5] Anja A. Kühl,[10] Carl Weidinger,[6] TRR241 IBDome Consortium, Rolf Backofen,[3,11] Ahmed N. Hegazy,[6,7] Jay V. Patankar,[4,5] and Christoph S.N. Klose[1,13,*]

[1]Charité – Universitätsmedizin Berlin, corporate member of Freie Universität Berlin and Humboldt-Universität zu Berlin, Department of Microbiology, Infectious Diseases and Immunology, Hindenburgdamm 30, 12203 Berlin, Germany
[2]Department of Visceral Surgery and Medicine, Inselspital, Bern University Hospital, University of Bern, Bern, Switzerland
[3]Bioinformatics Group, Department of Computer Science, University of Freiburg, Georges-Koehler-Allee 106, 79110 Freiburg, Germany
[4]Department of Medicine 1, Universitätsklinikum Erlangen and Friedrich-Alexander-Universität Erlangen-Nuremberg (FAU), Erlangen, Germany
[5]Deutsches Zentrum Immuntherapie (DZI), Erlangen, Germany
[6]Charité – Universitätsmedizin Berlin, corporate member of Freie Universität Berlin and Humboldt-Universität zu Berlin, Department of Gastroenterology, Infectious Diseases and Rheumatology, Hindenburgdamm 30, 12203 Berlin, Germany
[7]Deutsches Rheuma-Forschungszentrum, a Leibniz Institute, 10117 Berlin, Germany
[8]Picower Institute for Learning and Memory, Massachusetts Institute of Technology, Cambridge, MA, USA
[9]Department of Brain and Cognitive Sciences, Massachusetts Institute of Technology, Cambridge, MA, USA
[10]Charité – Universitätsmedizin Berlin, corporate member of Freie Universität Berlin and Humboldt-Universität zu Berlin, iPATH.Berlin-Immunpathologie für Experimentelle Modelle, Hindenburgdamm 30, 12203 Berlin, Germany
[11]Signalling Research Centres BIOSS and CIBSS, University of Freiburg, Schaenzlestr. 18, 79104 Freiburg, Germany
[12]These authors contributed equally
[13]Lead contact
*Correspondence: christoph.klose@charite.de
https://doi.org/10.1016/j.neuron.2025.02.018

## SUMMARY

Enteric infections often cause long-term sequelae, including persistent gastrointestinal symptoms, such as pain, discomfort, or irritable bowel syndrome. The plethora of sensory symptoms indicates that gut-innervating neurons might be directly affected by inflammation. However, sequencing studies of neurons in the gastrointestinal tract are hampered by difficulties in purifying neurons, especially during inflammation. Activating a nuclear GFP tag selectively in neurons enabled sort purification of intrinsic and extrinsic neurons of the gastrointestinal tract in models of intestinal inflammation. Using bulk and single-nucleus RNA sequencing, we mapped the whole transcriptomic landscape and identified a conserved neuronal response to inflammation, which included the interferon signaling and ferroptosis pathway. Deletion of the interferon receptor 1 in neurons regulated ferroptosis, neuronal loss, and consequently gut-transit time. Collectively, this study offers a resource documenting neuronal adaptation to inflammatory conditions and exposes the interferon and ferroptosis pathways as signaling cascades activated in neurons during inflammation.

## INTRODUCTION

The nervous and immune systems, which act as our body's main sensory interfaces, constantly monitor homeostasis and can mount an effector response upon challenge. However, how these systems exchange information to coordinate such a response, particularly at the mucosal barrier of the gastrointestinal (GI) tract, remains elusive. The GI tract has its own nervous system, the enteric nervous system (ENS), which represents the largest accumulation of neurons outside the central nervous system (CNS). The ENS mediates intestinal motility and fluid secretion largely autonomously from CNS control.[1,2] The intestine is also innervated by extrinsic neurons, conveying feedback signals to and from the CNS.

Enteric neurons emerge as regulators of immune responses within the GI tract at steady state and during instances of inflammation.[3–11] Conversely, the nervous system serves as a direct receiver of inflammatory signals through the expression

*(legend on next page)*
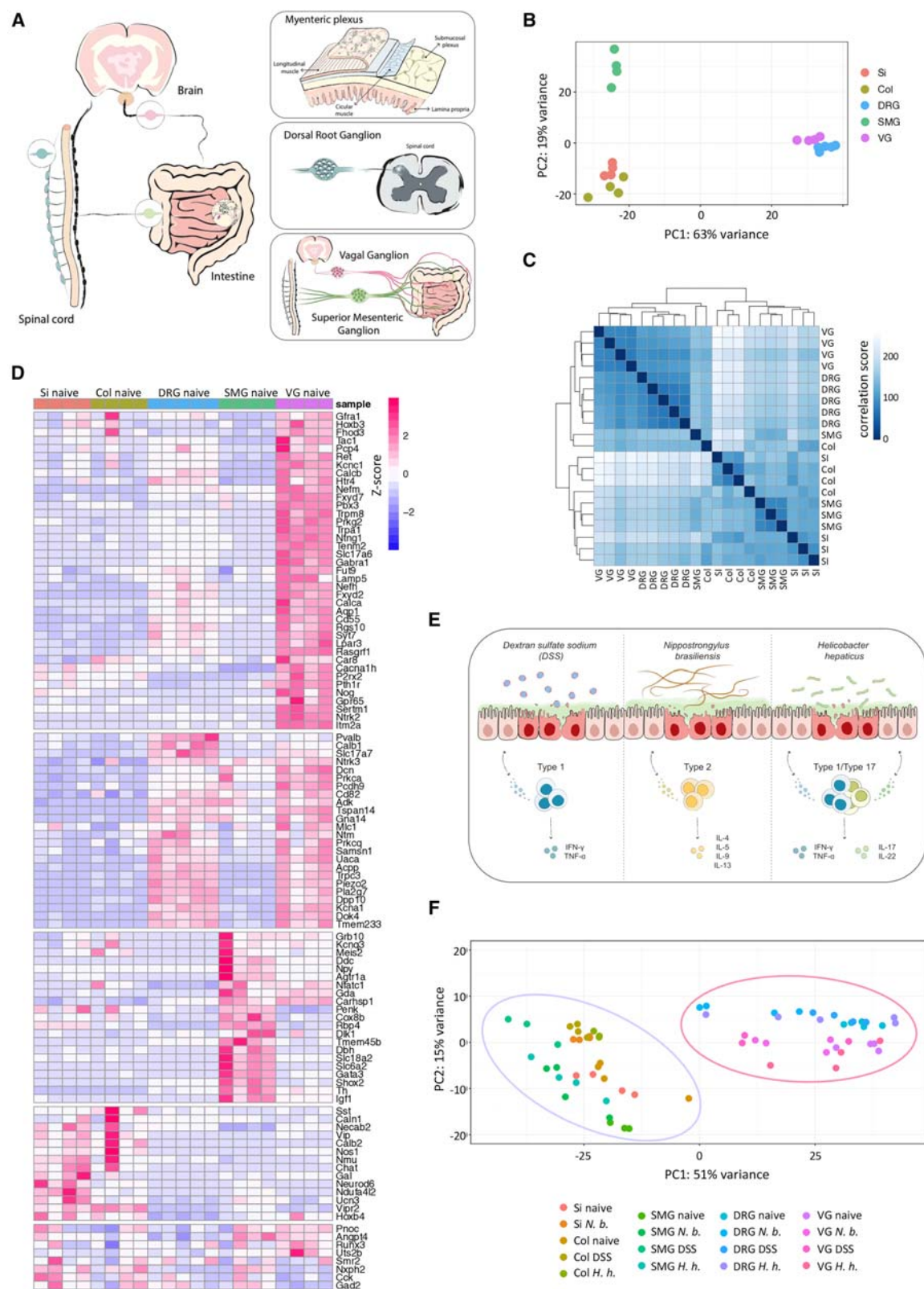
# Neuron
## NeuroResource

of cytokine receptors, thereby directly influencing neuronal structure and function in both, the peripheral nervous system (PNS) and CNS.[12–14] In fact, persistent GI symptoms following inflammation, which include abdominal pain or irritable bowel syndrome (IBS), can affect up to 40% of the world's population,[15] suggesting profound changes in neuronal circuits. Indeed, enteric neurons have been observed to undergo cell death post-infection.[16] Different types of cell death have been described, including non-apoptotic ferroptosis, an iron-dependent type of necrosis triggered by extensive membrane damage due to lipid peroxidation and subsequent loss of membrane integrity.[17] Ferroptosis was observed in neurons in the CNS in the context of neurodegeneration, ischemic stroke, or ischemia-reperfusion injury, which have a strong inflammatory component. However, how this specific type of cell death affects the ENS remains to be explored.

Although several studies have characterized the transcriptome of the ENS at steady state,[18–21] the molecular signaling pathways triggered in neurons by inflammation remain unexplored. Here, we generated an RNA sequencing atlas of intrinsic and extrinsic neurons innervating the GI tract following Th1-, Th2-, and Th17-skewing intestinal inflammation models. Inflammation induced a conserved program in both, intrinsic and extrinsic neurons, which was independent of the stimulated cytokine milieu. Under inflammatory conditions, GI-innervating neurons underwent ferroptosis, a type of non-apoptotic cell death. Ferroptosis induction was dependent on the direct sensing of type 1 interferons (IFNs) by neurons since conditional deletion of the IFN receptor alpha 1 (Ifnar1) in neurons diminished ferroptosis, neuronal loss, and gut-transit time, suggesting that this pathway may display a target for the treatment of long-term symptoms associated with neuronal loss in the GI tract.

## RESULTS

### The gene expression profile of GI-innervating neurons is primarily driven by its anatomic location and function

To sort-purify neuronal nuclei at steady state and during inflammation, we used the isolation of nuclei tagged in specific cell types (INTACT) mouse system, which allows for the Cre-induced expression of GFP fused to the nuclear protein Sun1.[22] The INTACT (Rosa26^Sun1-Gfp/Sun1-Gfp) mouse line was crossed to the Snap25^Cre/+ mouse line, which expresses Cre-recombinase under the Snap25 promoter and reliably labels all neurons,[23] also in the intestine.[24] The organs containing the neuronal somata of the intrinsic and extrinsic innervation, such as the intestine, the superior mesenteric ganglion (SMG), the vagal ganglia (VGs), and dorsal root ganglia (DRGs) were dissected from Snap25^Cre/+

Rosa26^Sun1-Gfp/+ mice (Figures 1A and S1A). The nuclei were extracted and sorted to approximately 98% purity via fluorescence-activated cell sorting (FACS) (Figures S1B and S1C). Validation of sort-purified nuclei from the myenteric plexus of the small intestine by RNA sequencing showed a clear enrichment of neuronal genes known to be expressed in the ENS, such as Snap25, Vip, Nmu, and Chat in GFP⁺ compared with GFP⁻ nuclei, which was also confirmed by qPCR (Figures S1D–S1F). Genes encoding for immune cells or glia cells, such as Ptprc or Gfap, were not detected in GFP⁺ nuclei in steady state and during inflammation, arguing against contamination of non-neuronal cells (Figure S1G). To detect the transcriptional profile of neuronal nuclei innervating the GI tract, we isolated the myenteric plexus from the small intestine and the colon, the DRGs, the SMG, and the VG, and performed bulk RNA sequencing (Figures 1B–1D). First, we detected an organ-specific transcriptional signature revealing a close transcriptional relationship between intrinsic and extrinsic sensory neurons (DRG and VG) (Figures 1B and 1C). The SMG showed a mixed sensory and effector transcriptional profile, suggesting its dual role in sensing and executing certain signals. Next, we examined the expression of neuronal markers from the myenteric plexus,[19] DRGs,[25–27] SMG,[28] and VG[29] (Figure 1D). The myenteric plexus showed expression of Vip, its receptor Vipr2, Chat, Nos1, and Nmu, which have immunoregulatory functions[3,4,8,9,30,31] (Figure 1D). The DRGs and the VG expressed genes linked to sensory neurons, such as Pvalb, Calca, or Nefh. Both anatomic sites showed enrichment of genes encoding for myelinated neurons, such as Nefh, or genes marking peptidergic (PEP) and non-peptidergic (NP) neurons, such as Tac1, Trpm8, and Calcb. The SMG showed genes enriched in the sympathetic nervous system, such as Npy and Th (Figure 1D). To test whether these molecular signatures may get altered following inflammatory triggers, we compared the results to models of intestinal inflammation. We chose three different models affecting distinct segments of the GI tract and eliciting preferentially either a Th1, Th2, or Th17-dominated response to assess the impact of the cytokine milieu (Figure 1E). These models included dextran sulfate sodium (DSS)-induced colitis dominated by a type 1 cytokine milieu (Figures S1H and S1I), worm infection with Nippostrongylus brasiliensis (N. brasiliensis) triggering a type 2 response (Figures S1J–S1L), and Helicobacter hepaticus (H. hepaticus)-induced colitis, characterized by a type 1/Th17 pathology (Figure S1M). The sequencing results of the GI innervation revealed a conserved transcriptional signature independent of the type of inflammation triggered but strongly driven by the anatomical location (Figure 1F). Therefore, GI-innervating neurons harbor a tissue- and location-specific gene expression signature largely maintained during inflammation.

**Figure 1. The transcriptional profile of neurons is shaped by its anatomic location**

(A) Illustration of neuronal segments analyzed.

(B) Principal-component analysis (PCA) of bulk RNA-seq of nuclei isolated from Si, Col, DRG, SMG, and VG of naive Snap25^Cre/+ Rosa26^Sun1-Gfp/+ mice.

(C) Sample-to-sample-distance plot showing correlation of the samples shown in (B).

(D) Heatmap of neuronal marker genes of same samples as in (B).

(E) Illustration of disease models. Mice were treated with DSS, infected with N. b. or infected with H. h. to elicit different types of inflammation.

(F) PCA of bulk RNA-seq of nuclei isolated from Si, Col, DRG, SMG, and VG of Snap25^Cre/+ Rosa26^Sun1-Gfp/+ mice, naive or infected with DSS, N. b. or H. h. For (B)–(D) and (F), each symbol or heatmap column represents data from one mouse. Si, small intestine; Col, colon; DRGs, dorsal root ganglia; SMG, superior mesenteric ganglion; VG, vagal ganglion; DSS, dextran-sulfate-sodium-induced colitis; N. b., Nippostrongylus brasiliensis; H. h., Helicobacter hepaticus.
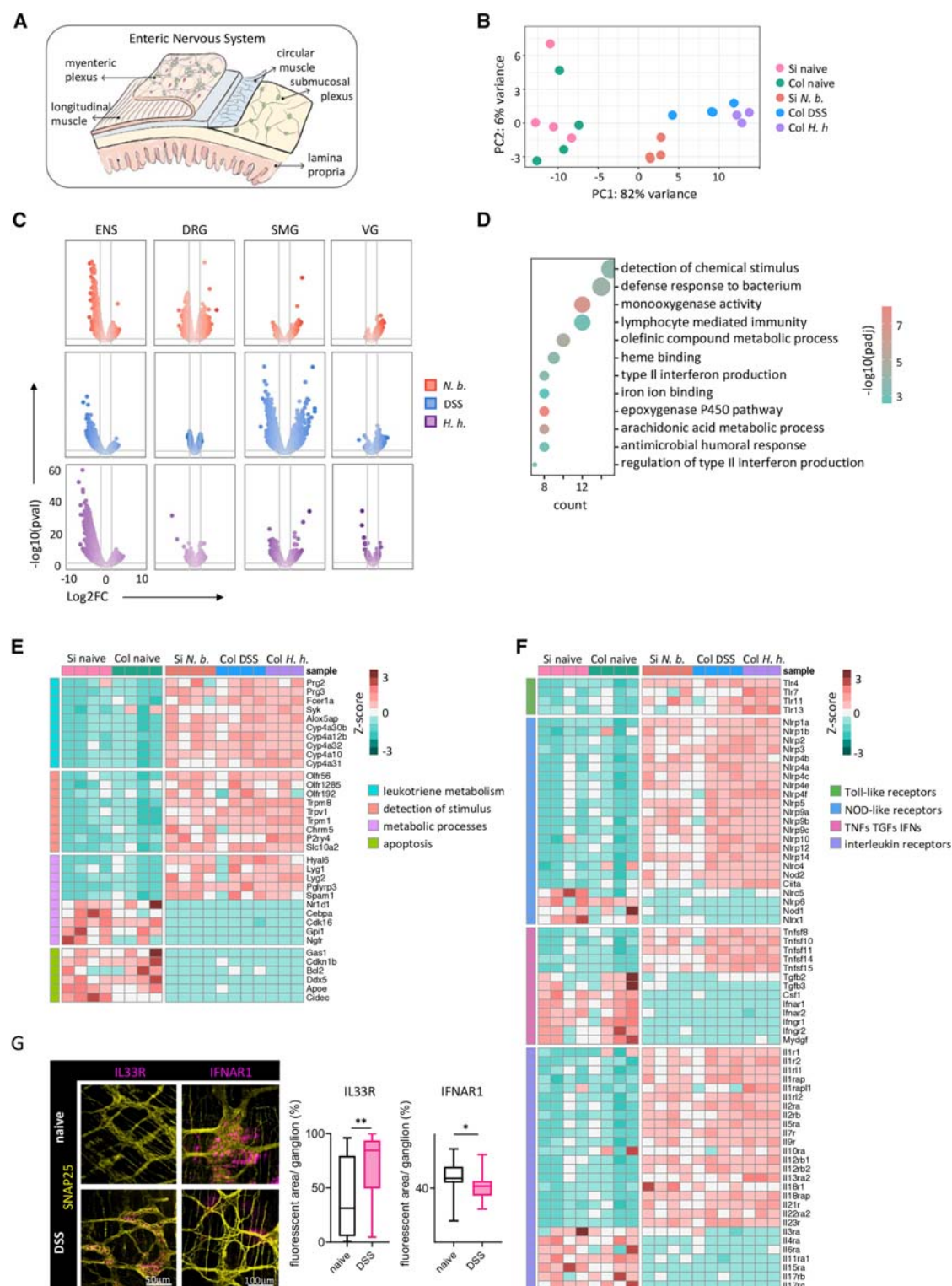
**Figure 2. Myenteric neurons upregulate sensory and effector modules during inflammation**

(A) Illustration showing the ENS.

(B) PCA of bulk RNA-seq of nuclei isolated from myenteric plexus of Si and Col of naive and infected *Snap25*<sup>Cre/+</sup> *Rosa26*<sup>Sun1-Gfp/+</sup> mice.

(C) Volcano plots showing transcriptional changes across all neuronal samples and disease models.

(D) Gene Ontology (GO) analysis of upregulated genes during inflammation in the myenteric plexus.

*(legend continued on next page)*

# Neuron
## NeuroResource

## Myenteric neurons show a shared inflammatory response profile across different models of inflammation

To explore the neuronal response triggered in the myenteric plexus during intestinal inflammation, we analyzed the transcriptional responses in myenteric neurons of the small intestine during *N. brasiliensis* infection, and the colon in DSS-induced and *H. hepaticus*-induced colitis models (Figure 2A). Principal-component analysis indicated apparent transcriptional changes in neurons from the small intestine and colon compared with non-inflamed neurons in the same regions (Figure 2B). Similar molecular alterations were observed in myenteric neurons independent of the disease models and intestinal location, suggesting a conserved neuronal response of myenteric neurons to inflammation (Figures 2B, 2C, S2A, and S2B). Comparison of transcriptional responses across intrinsic and extrinsic neurons revealed that the response was primarily driven by the anatomic proximity to the inflammatory milieu (Figure 2C). To explore signaling pathways in myenteric neurons during inflammation, we performed pathway analysis using the Gene Ontology Biological Process (GO:BP) dataset. Upregulated pathways across all inflammation models included "detection of chemical stimuli" and several immune-related pathways, such as "defense response to bacteria" and "lymphocyte mediated immunity," indicating a direct involvement of neurons in sensing and coordinating the inflammatory response (Figure 2D). In contrast, downregulated pathways included "axonogenesis," "dendrite development," and "signal release from the synapse," suggesting that the inflammatory milieu may impose structural alterations to the myenteric plexus (Figure S2C).

Additionally, we identified "leukotriene metabolism," "detection of stimulus," "metabolic processes," and "apoptosis" as regulated pathways (Figure 2E). Leukotriene metabolism together with arachidonic acid metabolism and the epoxygenase P450 pathway identified myenteric neurons as potential source of inflammatory mediators (Figures 2D and 2E). We could observe a metabolic shift from glucose utilization as an energy source toward the cellular use of lipids (Figures 2D, 2E, and S2C). However, those pathways were linked to the generation of inflammatory lipid mediators and lipid peroxidation. Notably, apoptosis-related genes showed decreased expression. Furthermore, pathways related to the sensing of molecules were upregulated, including chemical, cytokine, or pattern recognition receptor (PRR) signaling pathways. Differentially expressed genes under the GO term "detection of stimuli" included olfactory receptors, such as *Olfr56*, originally described in the olfactory epithelium, but also expressed in other cell types, including neurons (Figures 2E and S2D),[32] suggesting a potential role in metabolite sensing. The transient receptor potential (TRP) channels *Trpv1* and *Trpm8*, previously linked to inflammatory bowel disease (IBD), were also induced during inflammation at both, the tran-

scriptional and protein level (Figures 2E and S2D). Several Toll-like, NOD-like, and interleukin receptors were differently regulated following inflammation (Figure 2F). The regulation of inflammasome components by myenteric neurons implies active recognition of pathogen- and danger-associated molecular patterns (Figure 2F), and the regulation of cytokine receptors *Il1r1*, *Il1rl1*, *Il18r1*, and *Il23r*, indicates neuronal sensing of cytokines (Figures 2F, 2G, and S2D). In contrast, type 1 and 2 IFN receptor signaling pathways, including *Ifnar1*, *Ifnar2*, *Ifngr1*, and *Ifngr2*, were downregulated suggesting that IFNs could stimulate cell-intrinsic immunity in neurons[33] (Figures 2F and 2G). Complementing to shared signaling circuits, we plotted unique pathways and genes for each inflammation model, which were most pronounced during *N. brasiliensis* infection (Figures S3A–S3G). Taken together, these data expose the ENS as an active participant in inflammation independent of the inflammatory milieu, indicating that basal inflammatory cues drive the myenteric neuronal response.

## Different neuronal populations in DRGs contain the machinery necessary for sensing inflammatory cues

The *extrinsic* innervation of the GI tract includes DRG neurons sending bifurcating axons to the intestine, which detect distension, inflammation, and visceral stimuli (Figure 3A). We performed RNA sequencing on all thoraco (T1–13)-lumbar (L1–L6) DRGs at steady state and during intestinal inflammation. Since we observed pronounced differences in DRG neurons during *N. brasiliensis* infection compared with colitis models (Figures 2C, 3B, S4A, and S4B), we focused our analyses on delineating those transcriptional changes. GO enrichment analysis showed activation of pathways involved in the regulation and initiation of immune responses, production of inflammatory mediators and lipid metabolism, such as "olefinic compound metabolic processes," "eicosanoid metabolic processes," "arachidonic acid metabolism," and the "epoxygenase P450 pathway," consistent with previous data from myenteric neurons (Figures 2D, 2E, and 3C). Several cytokine and chemokine, Toll-like, and NOD-like receptors were differently regulated (Figures 3D and S4A), suggesting that DRGs sense immunological cues. Some of the regulated receptors are involved in neuro-immune crosstalk and play important roles in pain perception and behavior.[34–37] Similar to myenteric neurons, IFN receptors *Ifnar1*, *Ifnar2*, *Ifngr1*, and *Ifngr2* were downregulated following helminth infection (Figures 3D and 3E). We further found expression of C-type lectin domain receptors in DRG neurons (Figure 3D). Immunofluorescent validation of IFNAR1 and Toll-like receptor (TLR)4 in both, steady state and during *N. brasiliensis* infection, confirmed protein expression (Figures 3E and S4C). To assess different populations of neurons, we performed 10× single-nucleus sequencing of DRGs in steady state and following *N. brasiliensis* infection (Figures 3F, 3G, and S4D). We validated our neuronal purification strategy by searching for contaminating

---

(E and F) Heatmaps of dysregulated genes during inflammation in the myenteric plexus. (E) Different pathway-associated genes, (F) immune-related genes. For (B), (E), and (F), each symbol or heatmap column represents data from one mouse.

(G) Immunofluorescence staining of whole mounts colonic muscularis showing interleukin (IL)-33R/IFNAR1 (magenta) and SNAP25 (yellow). Quantification was performed measuring the % area of the protein of interest (IL-33R: naive $n = 5$, DSS $n = 5$; IFNAR1: naive = 5, DSS = 8, data are representative of two independent experiments). Si, small intestine; Col, colon; ENS, enteric nervous system; DRGs, dorsal root ganglia; SMG, superior mesenteric ganglion; VG, vagal ganglion; DSS, dextran-sulfate-sodium-induced colitis; *N. b.*, *Nippostrongylus brasilienis*; *H. h.*, *Helicobacter hepaticus*. Mean ± SD, Student's t test. *$p < 0.05$, **$p < 0.01$.
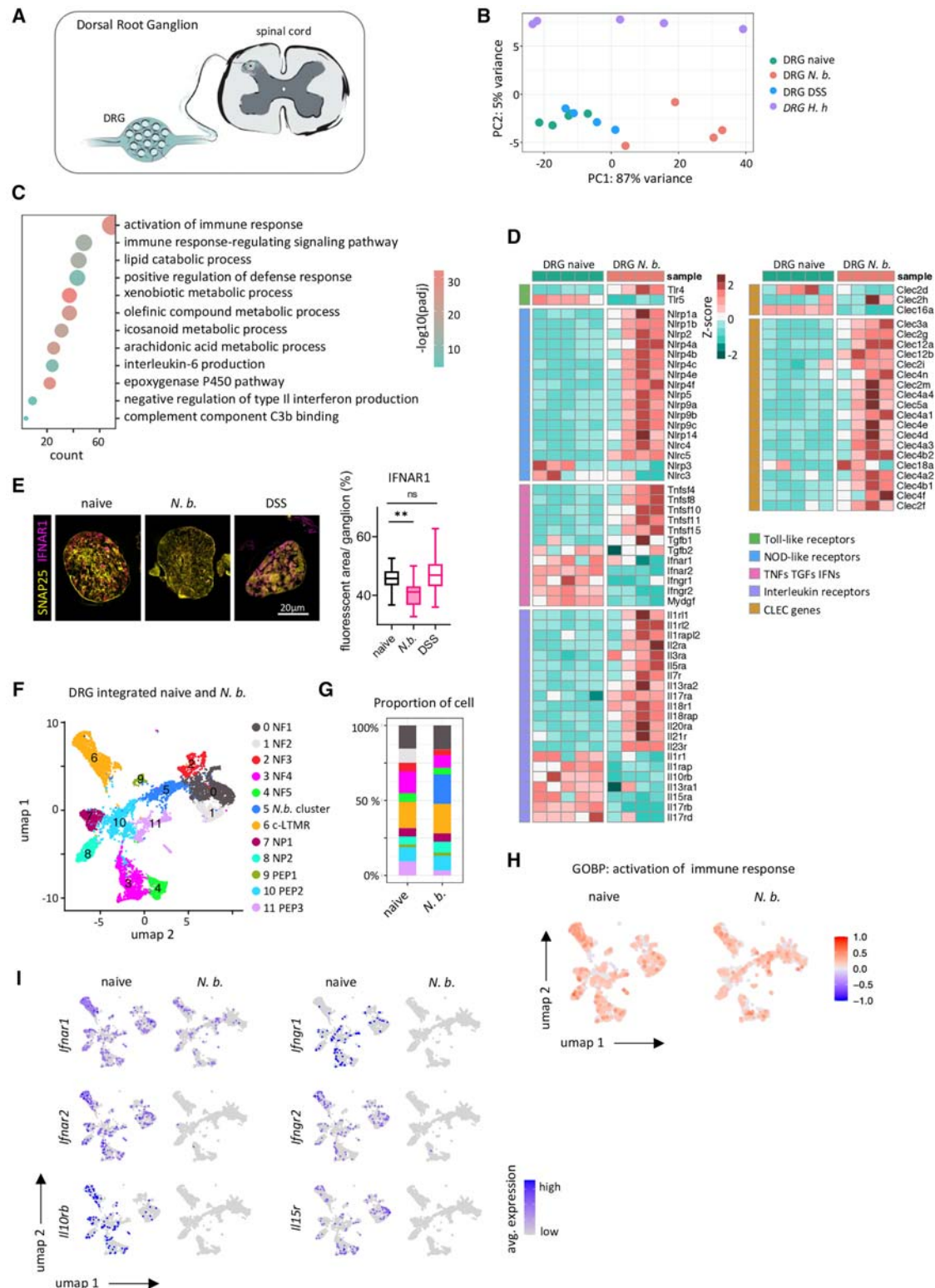
**Figure 3. The sensory DRGs are primarily involved in the perception of worm infection**

(A) Illustration of the anatomy of DRG.

(B) Principal component analysis of bulk RNA-seq of nuclei isolated from DRG of naive and infected Snap25^Cre/+ Rosa26^Sun1-Gfp/+ mice.

(C) Gene Ontology (GO) analysis of N. b.-induced upregulated genes in DRG.

*(legend continued on next page)*

immune cells (Figure S4E). None of those markers were detected in the single-nucleus dataset underpinning the clean strategy used for sort purification. Cluster annotation based on published datasets with specific functional annotations[26,38] revealed the representation of known neurofilamentous (NF), peptidergic (PEP), and non-peptidergic (NP) neuronal sub-clusters. We detected 5 NF populations, one low-threshold mechanoreceptor cluster expressing *Th*, two NP nociceptor clusters expressing *Mrgprd* and *Il31rα*+, *Npy2r*+, respectively, one *Trpm8*+ PEP cluster, and two PEP clusters characterized by the expression of *Trpv1*, *Tac1*, or *Calca*, respectively (Figures 3F, 3G, and S4F) These findings are in line with previous single-cell datasets of sort-purified DRG neurons[25,26,38,39] (Figure S4G) and specifically colon-innervating DRGs, suggesting that a broad array of sensory neurons was captured (Figures S4G, S5A, and S5B).[39] While mapping neurons after *N. brasiliensis* infection versus steady state, we identified the *de novo* occurrence of a neuronal cluster (Figures 3F and 3G). Detailed analysis of this transcriptionally unidentified cluster through comparison of its gene regulation with known clusters, revealed a population of neurons characterized by high metabolic activity and stress-related gene expression (Figures S5C and S5D). These results suggest that *N. brasiliensis* infection induced transcriptional stress, potentially due to their high activity. Next, we mapped pathways and genes in subpopulations of neurons in steady state and during *N. brasiliensis* infection. The pathway "activation of immune response" was found in all populations of DRG neurons, indicating that all DRG neuron subtypes responded to inflammation (Figure 3H). We found robust expression of *Ifnar1*, encoding the receptor for type 1 IFNs, at steady state in Th+ C-low threshold mechano receptors (LTMRs) neurons but also other neuronal populations. During *N. brasiliensis* infection, expression of IFN receptors (*Ifnar1/2*, *Ifngr1/2*) was downregulated across the different populations (Figure 3I). This was also observed for *Il10rb* and *Il15ra*, suggesting that the expression and detection of cytokine stimuli are regulated in different neuronal subtypes (Figure 3I).

In summary, data from bulk and single-nucleus sequencing under different inflammatory conditions revealed that neurons express and regulate cytokine and chemokine receptors, supporting the notion that neurons possess an inflammation-detection machinery.

## SMG neurons are strongly activated in response to inflammation

We extended our analysis of the *extrinsic* innervation of the GI tract on the sympathetic and parasympathetic arm of the autonomic nervous system, both being functional counterplayers

and exerting opposing effector functions. To gain detailed insights into regulated programs in response to inflammatory stimuli in both systems, we isolated the SMG, which functions as post-ganglionic neurons of the sympathetic nervous system, and the parasympathetic VG, consisting of vagal somatic and visceral sensory afferent neurons (Figure 4A). RNA sequencing and analysis of differentially regulated genes in steady state versus inflammation showed differences in gene expression in both, the SMG and VG, particularly during colitis, with smaller differences in the parasympathetic VG (Figures 4B and S6A–S6D). Thus, at the transcriptional level, the sympathetic nervous system showed a stronger response during inflammatory conditions compared with the parasympathetic VG. In line with our previous results in other neurons (Figures 2 and 3), differential GO expression analysis of SMG neurons showed upregulation of immune response pathways ("lymphocyte mediated immunity," tumor necrosis factors [TNFs], TNF receptors), sensory signaling ("detection of chemical stimulus," "olfactory signaling pathway"), inflammatory mediator production, and lipid metabolism pathways ("linoleic acid metabolic processes," and the "epoxygenase P450 pathway") significantly upregulated following colitis (Figures 4C and 4D). Consistent with the results obtained in myenteric neurons, immunological molecules of Toll-like, NOD-like, and cytokine receptor families (*Ifnar1*, *Ifnar2*, *Ifngr1*, and *Ifngr2*) were differently regulated, particularly in the SMG (Figure 4D). Comparable pathways were observed in the VG, suggesting that the overall neuronal response is similarly adapted across different neuronal components (Figures 4D and S6E). To further investigate gene regulation at the cellular level, we performed single-nucleus sequencing of sort-purified nuclei from *Snap25*Cre/+ *Rosa26*Sun1-Gfp/+ mice at steady state and during DSS-induced colitis in the SMG and VG. We detected pure neurons, free of contamination by immune or glial cells, suggesting that the bulk sequencing data obtained from SMG and VG were not contaminated by non-neuronal cells (Figures 4E, S6F, and S6G). In the SMG, we detected broad expression of pan-neuronal markers *Snap25* and *Tubb3* in all clusters, along with consistent expression of *Th* and *Npy* in all 6 clusters, underlining the SMG as key signaling hub of the sympathetic nervous system (Figures S7A–S7C).[40,41] Functional characterization of neuronal populations indicated a mix of sensory and effector neuronal modules based on their distinct neuronal profiles (Figure S7D). The VG dataset consisted of 11 neuronal clusters and the markers *Phox2b* and *Prdm12* allowed for the identification of nodose and jugular neuronal clusters as previously described (Figures 4E and S7E–S7H).[29] In line with the bulk RNA sequencing, VG neurons showed marker

(D) Heatmaps of *N. b.*-induced dysregulated genes showing immune-related (left) and CLEC genes (right). For (B)–(D), each symbol or heatmap column represents data from one mouse.

(E) Immunofluorescence validation of DRG sections showing IFNAR1 (magenta) and SNAP25 (yellow). Quantification was measured by % area of the protein of interest (naive $n = 5$, *N.b.* $n = 4$, DSS $n = 5$, data are representative of two independent experiments).

(F) Uniform manifold approximation and projection (UMAP) of single-nucleus RNA-seq from DRG combining naive and *N.-b.*-infected mice. 8 mice pooled per condition.

(G) Frequencies of cells per cluster from naive and infected samples shown in (F).

(H) UMAP showing genes enriched in the GO:BP pathway "activation of immune response" in naive versus *N. b.*-infected DRGs.

(I) UMAPs of *Ifnar1*, *Ifnar2*, *Ifngr1*, and *Ifngr2* expression in naive and *N.-b.*-infected DRGs. DRGs, dorsal root ganglia; DSS, dextran-sulfate-sodium-induced colitis; *N. b.*, *Nippostrongylus brasiliensis*; *H. h.*, *Helicobacter hepaticus*; CLEC, C-type lectin domain containing. Mean ± SD, one-way ANOVA. n.s., non-significant, *$p < 0.05$, **$p < 0.01$.

(legend on next page)

# Neuron
## NeuroResource
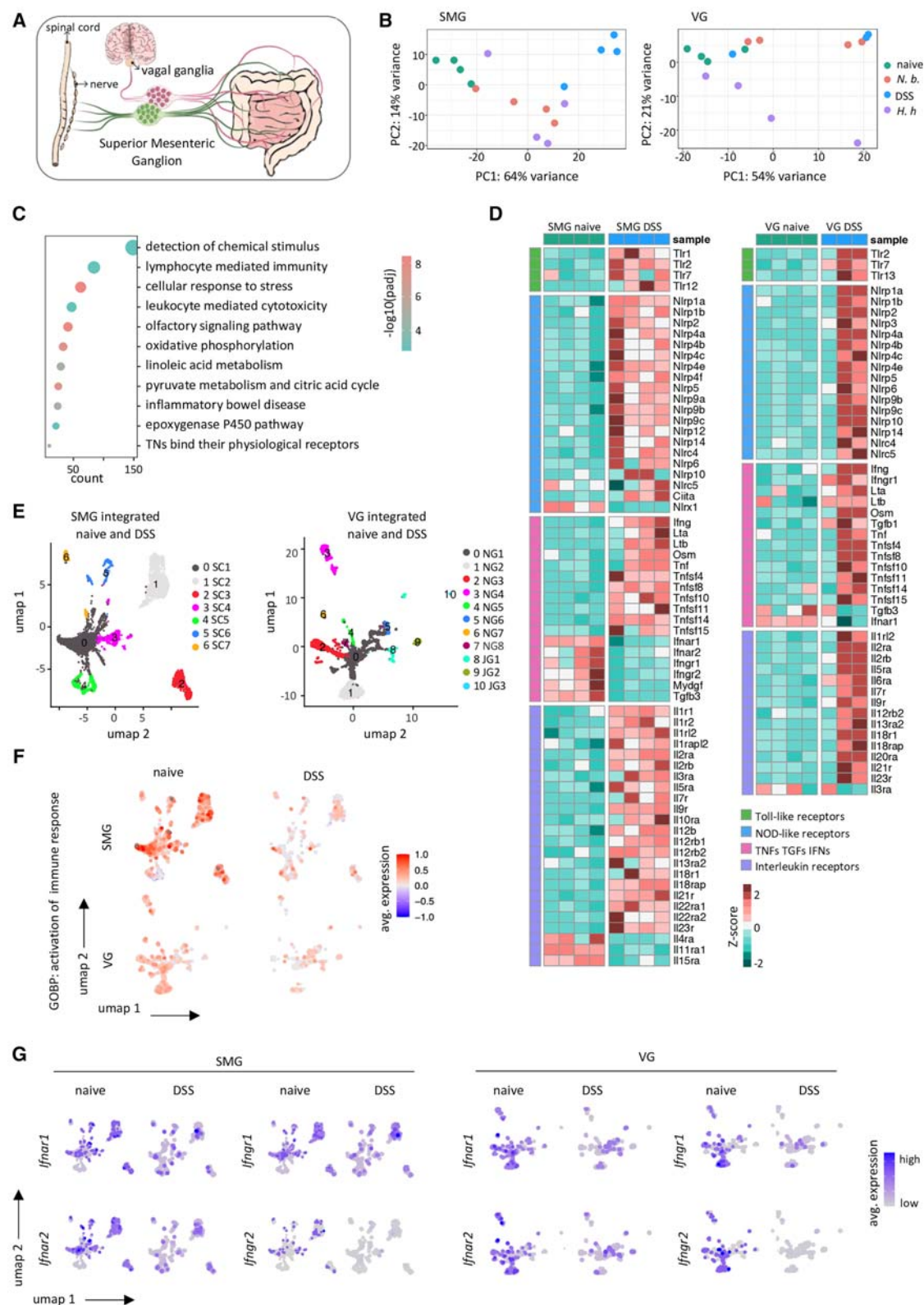
expression similar to DRGs, indicating that the VG is a sensory hub[29] (Figures S4F, S7E, S7G, S7H, S8A, and S8B). To this end, we compared the transcriptional profiles of DRG and VG neurons (Figures S8A–S8H). While both neuronal clusters shared similar neurochemical properties (Figures S8A and S8B), their physiological functions differ significantly. VG neurons showed enriched GO pathways, such as "response to hormone" or "regulation of blood pressure" when compared with DRGs (Figures S8D–S8F). In contrast, DRG neurons expressed genes representing "sensory perception of pain" or "neuropeptide signaling" compared with the VG (Figures S8D–S8F). These differences were also evident during inflammation (Figures S8G and S8H). Together, our data confirm the sensory nature of VG neurons while highlighting their distinct physiologic role. In the SMG, the activation of immune responses appeared to be found in all neuronal populations rather than being restricted to specific subsets. In contrast, the immune activation was relatively low in the VG (Figure 4F). Downregulation of IFN and cytokine receptors was consistently observed in both, SMG and VG (Figure 4G). In total, these data indicate that inflammation elicits a stronger sympathetic than parasympathetic transcriptional response and that a wide range of neurons are equipped with an inflammation-detection machinery.

## Jointly regulated pathways in neurons include the metabolism of linoleic acid, eicosanoids, arachidonic acid, and iron ion binding

Common pathways are triggered in neurons in various tissues and in different models of inflammation characterized by distinct cytokine profiles (Figures 2B–2F). We aimed to define those common pathways elicited in neurons as a consequence of inflammation. To achieve this, we focused on gene sets that exhibited differential regulation in at least one inflammation model across various neuronal tissues. This led to the identification of 12 protein clusters (Figure 5A) where the corresponding genes displayed diverse regulatory patterns across tissue-disease combinations (Figures S9 and S10). These patterns included both, shared pathways across different conditions and more variable expression patterns, that might reveal insights into tissue-specific regulation or differential activation levels within these pathways. We scrutinized gene sets potentially involved in common biological processes identified within the clusters (Figure 5A) spanning broader functional categories, such as synapse, signaling, receptors, and iron binding and lipid peroxidation metabolism (Figures 5B, S9, and S10). Synapses and neurotransmitters, in particular acetylcholine and adrenergic receptors, were altered during inflammation in clusters 1, 5, and 7. Additionally, immune and cytokine receptor activity, as

well as JAK-STAT signaling in cluster 10, and inflammatory mediators of the leukotriene receptors were enriched in cluster 4. The highest percentage of jointly regulated pathways falls in cluster 4, relating to the metabolism of retinol, linoleic acid, arachidonic acid, eicosanoid metabolism, and iron ion binding, along with inflammatory mediators of the TRP channels and leukotriene receptors (Figure 5B). Retinol metabolism potentially influences oxidative stress responses,[42] while linoleic acid serves as a precursor for arachidonic acid, which in turn contributes to the synthesis of leukotrienes as part of the broader context of eicosanoid metabolism. Therefore, these data argue that lipid metabolism might fuel the synthesis of leukotriene mediators in neurons, and dysregulation of the iron metabolism may promote the generation of reactive oxygen species.

## GI-innervating neurons show hallmarks of ferroptosis during intestinal inflammation

Unbound iron can promote the oxidation of polyunsaturated fatty acids via the Fenton reaction, resulting in lipid peroxidation.[17] Linoleic and arachidonic acid were described to stimulate lipid peroxidation, leading to ferroptosis.[43,44] To delineate the link between lipid metabolism, inflammatory mediators, and iron binding as jointly regulated pathways, we analyzed genes of the underlying ferroptosis-related pathways, lipid peroxidation, glutathione metabolism, iron metabolism, and the mevalonate pathways. Indeed, they were altered in all innervating sites, including upregulation of the arachidonic acid lipoxygenases *Alox5* and *Alox15*, promoting lipid peroxidation and ferroptosis (Figures 6A and 6B). Complementary, we observed downregulation of glutathione peroxidase 4 (*Gpx4*) and glutathione synthetase (*Gss*), which reduce lipids, as well as *Fth1*, which sequesters iron, and the iron-metabolism-regulating protein *Ireb2* (Figures 6A and 6B).

Since the gene expression analysis supports the idea that ferroptosis is induced in GI-innervating neurons upon inflammation, we investigated whether DSS-induced colitis results in cell death of myenteric neurons. Indeed, we found increased TUNEL+ neurons indicating that programmed cell death is induced (Figure 6C).[45,46] Since the apoptotic pathway was downregulated in the inflamed myenteric plexus (Figure 2C), we explored ferroptosis in myenteric neurons by staining for 4-hydroxynonenal (4-HN), a well-established product of lipid peroxidation and marker of ferroptosis. Consistent with our hypothesis, we detected increased 4-HN deposition in SNAP25+ neurons, which implies that the ongoing lipid peroxidation induces ferroptosis in these cells[17] (Figure 6D). In addition, we could confirm a decrease in GPX4 protein following DSS-induced colitis in myenteric neurons, providing evidence for the loss of the cellular glutathione-mediated antioxidant

---

**Figure 4. The SMG reacts and adapts its profile predominantly during acute Th1 inflammation**
(A) Illustration of the anatomic location of SMG and VG.
(B) PCA of bulk RNA-seq of nuclei isolated from SMG or VG of naive and infected *Snap25*[Cre/+] *Rosa26*[Sun1-Gfp/+] mice.
(C) Gene Ontology (GO) analysis of DSS-upregulated genes in SMG.
(D) Heatmap of immune-related genes dysregulated in SMG and VG. For (B)–(D), each symbol or heatmap column represents data from one mouse.
(E) UMAP of single-nucleus RNA-seq of SMG or VG, each plot combines the naive and DSS-treated sample. 5 mice for the naive and 10 mice for the DSS sample were pooled.
(F) UMAP showing genes enriched in the GO:BP pathway activation of immune response, conditions as in (E).
(G) UMAPs of *Ifnar1*, *Ifnar2*, *Ifngr1*, and *Ifngr2* expression in SMG and VG, conditions as in (E). SMG, superior mesenteric ganglion; VG, vagal ganglion; DSS, dextran-sulfate-sodium-induced colitis; *N.b.*, *Nippostrongylus brasiliensis*; *H.h.*, *Helicobacter hepaticus*.

*(legend on next page)*

# Neuron
## NeuroResource

CellPress
OPEN ACCESS
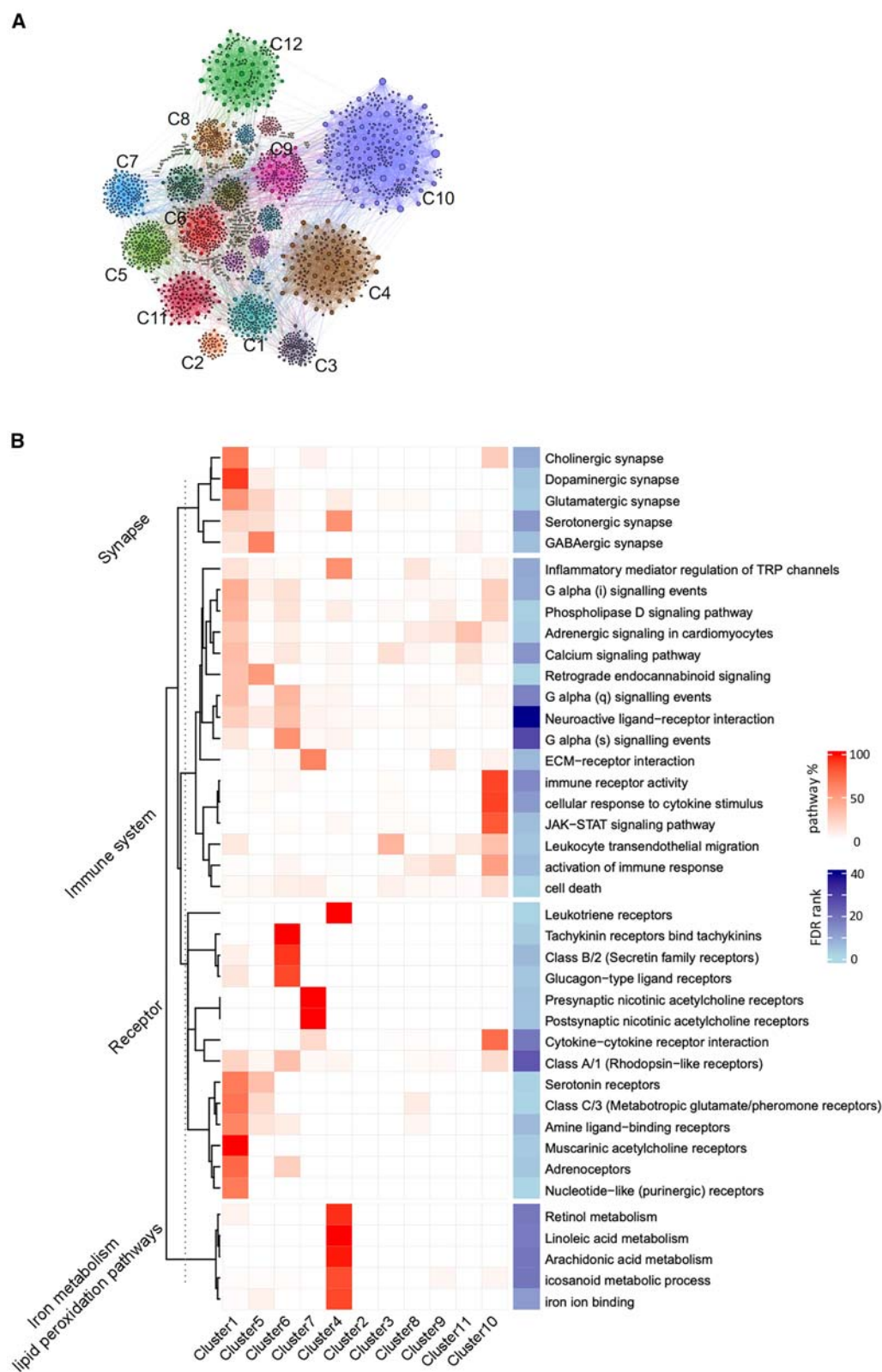
capacity and the consequent accumulation of reactive oxygen species (Figure 6D). While these data show that the ferroptosis pathway is activated in myenteric neurons *in vivo*, we assessed whether ferroptosis could be triggered in myenteric neurons *in vitro*. We exposed neuronal cultures to a combination of compounds known to promote ferroptosis.[47] Indeed, exposure to the ferroptosis-promoting cocktail resulted in increased uptake of propidium iodide (PI), an indicator of cell death, while addition of the ferroptosis inhibitor Liproxstatin-1 to the cultures prevented PI uptake (Figure 6E). Similar findings were obtained in DRG neurons following *N. brasiliensis* infection (Figures 6F and 6G) suggesting that ferroptosis induction in neurons involves intrinsic and extrinsic neurons of the GI tract. Taken together, our data indicate that inflammation promotes lipid peroxidation in GI-innervating neurons resulting in ferroptosis.

## IFN signaling regulates ferroptosis in neurons, leading to neuronal loss and altered gut-transit time

Our data indicate that ferroptosis is induced in neurons during inflammation and that neurons detect inflammation in part via the expression of cytokine and IFN receptors (Figures 2F, 2G, 3D, 3E, and 4D). Downregulation of certain cytokine receptors, such as the type 1 and 2 IFN receptors, may reflect receptor engagement followed by subsequent downregulation (Figures 2F, 2G, 3D, 3E, and 4D).[48,49] By measuring activated cytokine signaling pathways, we observed the induction of IFN response genes in myenteric neurons, confirming that the IFN signaling cascade was activated (Figure 7A). Similar findings were obtained in neurons representing the extrinsic innervation (Figures 7B and S11A). When neuronal cultures were exposed to type 1 IFN, we detected phosphorylation of STAT1 downstream of IFNAR1 (Figure 7C). Thus, type 1 IFN signaling and the ferroptosis pathway are triggered in parallel in neurons. Recent evidence suggests that type 1 IFN signaling can induce lipid peroxidation,[50] a key step in the induction of ferroptosis.[17] To expose signaling pathways regulated by type 1 IFNs in myenteric neurons, we generated a conditional deletion of *Ifnar1* in neurons while preserving an INTACT allele for sort purification of nuclei by crossing *Ifnar1*^{fl/fl} mice to a *Snap25*[Cre/+] *Rosa26*[Sun1-Gfp/+] background (*Snap25*[Cre/+] *Ifnar1*^{fl/fl} *Rosa26*[Sun1-Gfp/+], referred to as *Ifnar1*[ΔNeuron]). Western blot and immunofluorescence staining of DRG and myenteric neurons from *Ifnar1*[ΔNeuron] mice revealed the abrogation of IFNAR1 in neurons (Figures S11B–S11E). Analysis of bulk RNA sequencing data from neuronal nuclei at steady state showed that *Ifnar1* controlled the expression of numerous genes (Figures 7D and 7E). Differentially regulated pathways included fat metabolism, underpinning a role for *Ifnar1* in lipid metabolism (Figure 7E). To test whether type 1 IFNs are able to induce ferroptosis in neurons, we exposed myenteric neuronal cultures to IFN-β *in vitro*. IFN-β

was sufficient to elevate PI uptake, which could be inhibited by co-administration of Liproxstatin-1 (Figure 7F). Moreover, IFN-β synergized with erastin to promote ferroptosis, which could be blocked by addition of Ferrostatin (Figure S11F). Similar results were obtained by adding IFN-γ to myenteric neuronal cultures (Figure S11G). To test whether ferroptosis requires type 1 IFN signaling, we induced colitis in *Ifnar1*[ΔNeuron] and control mice via the administration of DSS and performed RNA sequencing on myenteric neurons (Figures 7G and 7H). *Ifnar1* deficiency influenced neurogenesis, neuron differentiation, and synapse organization (Figure 7H). Consistent with an important function of IFNAR1 in triggering ferroptosis, we observed that *Ifnar1*-deficient neurons failed to upregulate *Alox5*, and *Alox5ap* during colitis. In contrast, *Gpx4* and *Gss*, were only partially downregulated in *Ifnar1*-deficient neurons (Figures 7I, 7J, and S11H). Therefore, our data show that *Ifnar1* is involved in the regulation of ferroptosis in myenteric neurons. To assess the functional relevance of this finding, we performed chronic DSS-colitis experiments in *Ifnar1*[ΔNeuron] and littermate control mice. *Ifnar1*[ΔNeuron] mice lost less weight and had a longer colon compared with littermate controls (Figure 7K), arguing for a lower disease severity (Figures 7L and S11I). Immunofluorescent staining showed decreased 4-HN+ neurons and increased total numbers of neurons in mice lacking IFNAR1 (Figures S11J–S11L). As a consequence, gut motility was altered, as measured by a fluorescein isothiocyanate (FITC) dextran assay (Figure 7M). Overall, these data demonstrate an important role of neuronal IFNAR1 in regulating ferroptosis and, consequently, in modulating disease severity and gut-transit time.

To test the translational relevance of this finding, we correlated gene expression in samples from patients diagnosed with IBD with genes encoding for the ferroptosis pathway extending on previous data,[53] which demonstrated a link between *GPX4* and IBD. We found that *GPX4* negatively correlated with disease severity measured by the Naini-Cortina or the Riley score underpinning the exhaustion of GPX4 in concordance with IBD severity (Figure 7N). Next, we asked whether IFN signaling and ferroptosis are linked to human IBD. In line with the murine data, both genes, *IFNAR1* and *IFNGR1*, were negatively correlated with *GPX4*, providing evidence that these pathways are associated (Figure 7O). We could also detect 4-HN in NeuN+ neurons in human colitis samples but not control samples (Figure 7P). Thus, our findings may have implications for the prevention and therapy of sequelae in IBD.

## DISCUSSION

Infections are a vital threat to every organism, and a conserved inflammatory response has evolved to contain and combat them. Although the cardinal signs of inflammation are at least

**Figure 5. Conserved pathways across different anatomic locations**
(A) Protein network visualizing clusters of proteins where gene expression exhibits differential expression in at least one inflammatory model across various neuronal tissues. Each node represents a specific protein, while edges connecting the nodes depict associations between those proteins. The network employs color-coding to visually distinguish between different protein clusters based on their associations. This figure represents a protein interaction network derived from the String database.
(B) Heatmap of commonly dysregulated pathways across inflammation models and organs. False discovery rate (FDR) rank values: absolute value of the base $-\log_{10}$(FDR). This figure represents the identified pathways for each protein cluster derived from the protein interaction network shown in (A). Pathways are visualized as a heatmap with enrichment (pathway %) and FDR ranking.
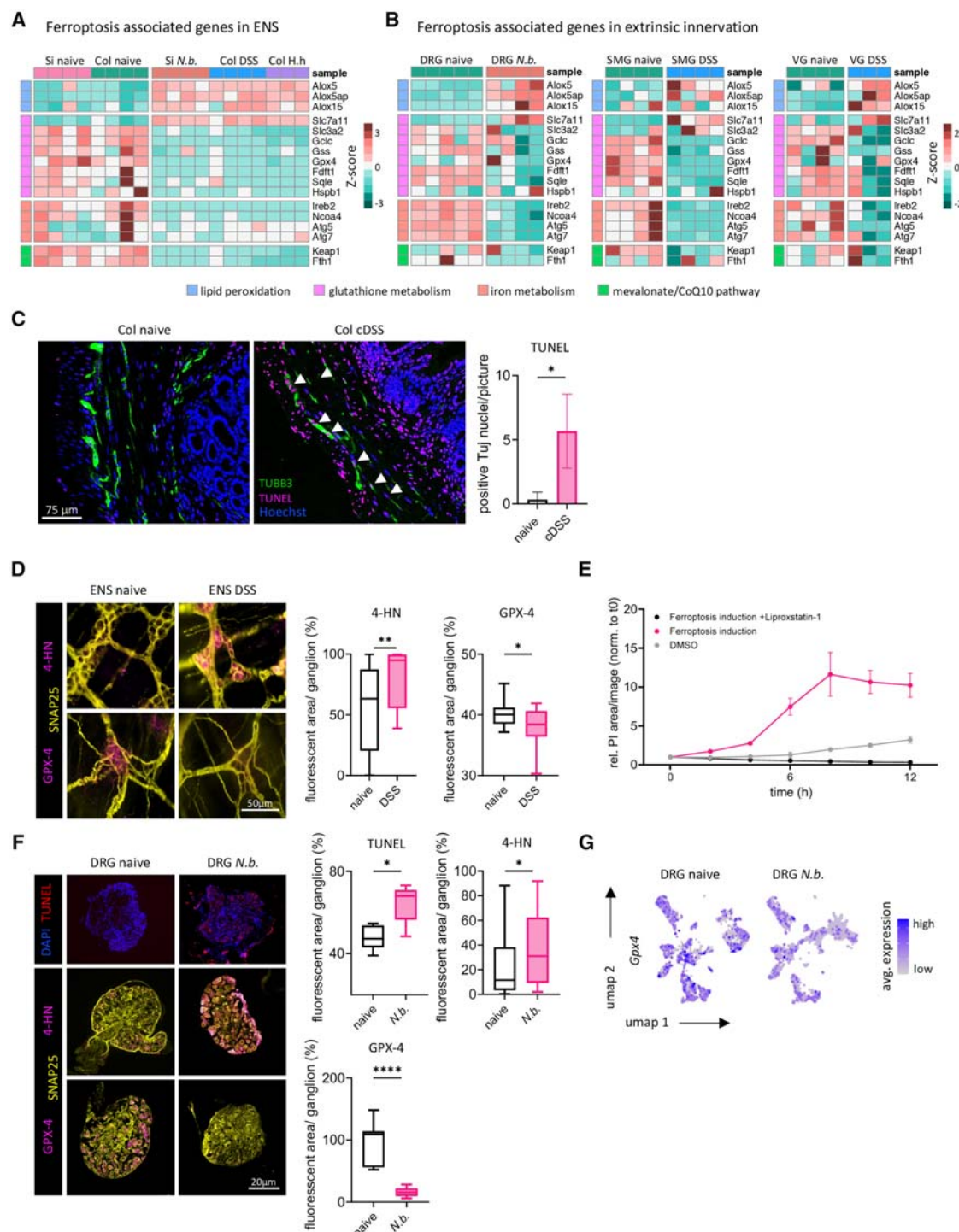
**Figure 6. Neurons display hallmarks of ferroptosis across all inflammation models**

(A) Heatmap showing ferroptosis-related genes in myenteric neurons from naive and infected $Snap25^{Cre/+}$ $Rosa26^{Sun1-Gfp/+}$ mice.

(B) Heatmaps showing ferroptosis-related genes in DRG during *N. b.*, in SMG and VG during DSS-induced colitis. For (A) and (B), each heatmap column represents data from one mouse.

(C) Immunofluorescence staining of colonic sections. TUNEL (magenta) and Tuj (green) stained in naive and chronic DSS. Quantification of TUNEL⁺ Tuj⁺ nuclei (per condition $n$ = 3–4 mice, data are representative of two independent experiments).

(D) Immunofluorescence staining of murine whole-mount muscularis showing 4-HN or GPX4 (magenta) and SNAP25 (yellow). Quantification was performed measuring the % area of the protein of interest (naive $n$ = 5, DSS $n$ = 8, data are representative of two independent experiments).

# Neuron
## NeuroResource

in part the consequence of neuronal activation, the neuron-inherent response and the associated transcriptional changes in neurons during inflammation are poorly understood.[54] Our study recognized a conserved neuronal response to inflammatory stimuli and demonstrated that neurons display hallmarks of immune sensing mechanisms through numerous means, including cytokine receptors, PRRs, and receptors for metabolites. We found arachidonic acid, eicosanoid, and leukotriene synthesis among the jointly regulated pathways. In addition, we discovered downregulation of IFN and other cytokine receptors, possibly due to receptor engagement. IFNs are key mediators of cell-intrinsic immunity to intracellular infections.[55] With regard to the nervous system, IFNs have been mainly studied in relation to immunity against neurotropic viral infections,[56,57] neurodegeneration,[58] and cognitive function in the CNS[59] or as a gatekeeper in nociceptors of the PNS controlling pain.[60]

An inevitable consequence of inflammation is tissue damage and cell death. Complementing necrosis and apoptosis reported in infected tissue,[61,62] our study identified ferroptosis as a substantial component of cell death triggered in neurons innervating the GI tract during inflammation.[17] Previous studies have found that pyroptosis, mediated by NOD-like receptor family pyrin domain-containing 6 (NLRP6) and caspase-11, is triggered in enteric neurons during intestinal inflammation.[16,63,64] While ferroptosis has been reported to exacerbate the course of colitis in mice and humans,[53,65] it has primarily been associated with epithelial cells.[53] Therefore, ferroptosis in enteric neurons may promote inflammation and tissue decline during colitis.

Apart from colitis, ferroptosis has been described in the nervous system in neurodegenerative diseases, such as Alzheimer's disease, Parkinson's disease, and amyotrophic lateral sclerosis.[66] Since we could link the IFN response in neurons to ferroptosis in the ENS, this pathway might contribute to disease's progression.

Our study's findings could provide a better understanding of GI disorders, such as IBD and IBS. Even subclinical infections of viral nature have been linked with initiation and chronicity of IBD.[67] Such infections may lead to persistent IFN signaling and thus may explain progressive decline of gut motor functions in IBD.

IBS is a common chronic GI disorders in Western countries often linked to enteric infection.[68] Hallmark symptoms of IBS include abdominal hypersensitivity, frequently manifesting as recurrent abdominal pain and abnormal bowel habits, which may be indicative of abnormal abdominal perception and alterations in the ENS.[14] Our research has identified that neurons undergo profound changes during intestinal infection, potentially leading to the development of IBS. Moreover, we have discovered that neurons, particularly myenteric neurons, undergo non-apoptotic cell death, independent of the inflammatory

trigger.[16] This finding, coupled with the correlation between IBS and parasitic intestinal infection[69] suggests the clinical relevance of our study. The conserved inflammatory pathway in neurons may pave the way for new strategies in preventing and treating GI disorders.

## Limitations of the study

This study was designed to identify the transcriptional landscape of neurons innervating the GI tract. Our analysis included in each case the entire organ, and, thus, may have diluted certain responses as some ganglia or neurons may be heavier affected by inflammation than others. To study components of the ENS and obtain high-quality neurons, the myenteric plexus was enriched whereas the submucosal plexus may be represented only to a minor degree in the sequencing dataset. It is likely that submucosal neurons, which are located even closer to the inflammatory milieu, may react even stronger to inflammatory triggers. The analysis of all thoracolumbar DRGs may have included neurons, which do not receive signals from the GI tract and therefore diluted the response. The inclusion of all thoracolumbar DRGs might explain the rather low transcriptional changes observed in DRGs during DSS-colitis. The ENS is composed of neurons and enteric glia, both of which are involved in inflammation. Future studies are required to address these cellular components in parallel. The colitis models contain a certain overlap in the induced cytokine milieu, including acute DSS-colitis with a predominate type 1 cytokine response but also a Th17 component[70–72] and the *H. hepatics* colitis model with a strong Th17 response, but IFN-γ production by T cells as well.[73–75]

(E) Enteric neuroglial cultures exposed to either arachidonic acid, RAS-selective lethal 3 (RSL3), and erastin alone (ferroptosis induction) or in combination with Liproxstatin-1 versus DMSO, monitored for propidium iodide uptake ($n = 3$).

(F) Immunofluorescence staining of murine DRGs showing protein of interest (magenta) and Snap25 (yellow). Quantification was performed as in (D) (naive $n = 5$, DSS $n = 5$, data are representative of two independent experiments).

(G) UMAP of *Gpx4* in DRG of naive and *N. b.*-infected *Snap25*$^{Cre/+}$ *Rosa26*$^{Sun1-Gfp/+}$ mice. ENS, enteric nervous system; Si, small intestine; Col, colon; DRGs, dorsal root ganglia; SMG, superior mesenteric ganglion; VG, vagal ganglion; DSS, dextran-sulfate-sodium-induced colitis; *N. b.*, *Nippostrongylus brasilienis*; *H. h.*, *Helicobacter hepaticus*. Mean ± SD, Student's t test (C–E) and two-way ANOVA (E). *$p < 0.05$, **$p < 0.01$, ***$p < 0.001$, ****$p < 0.0001$.

(legend on next page)
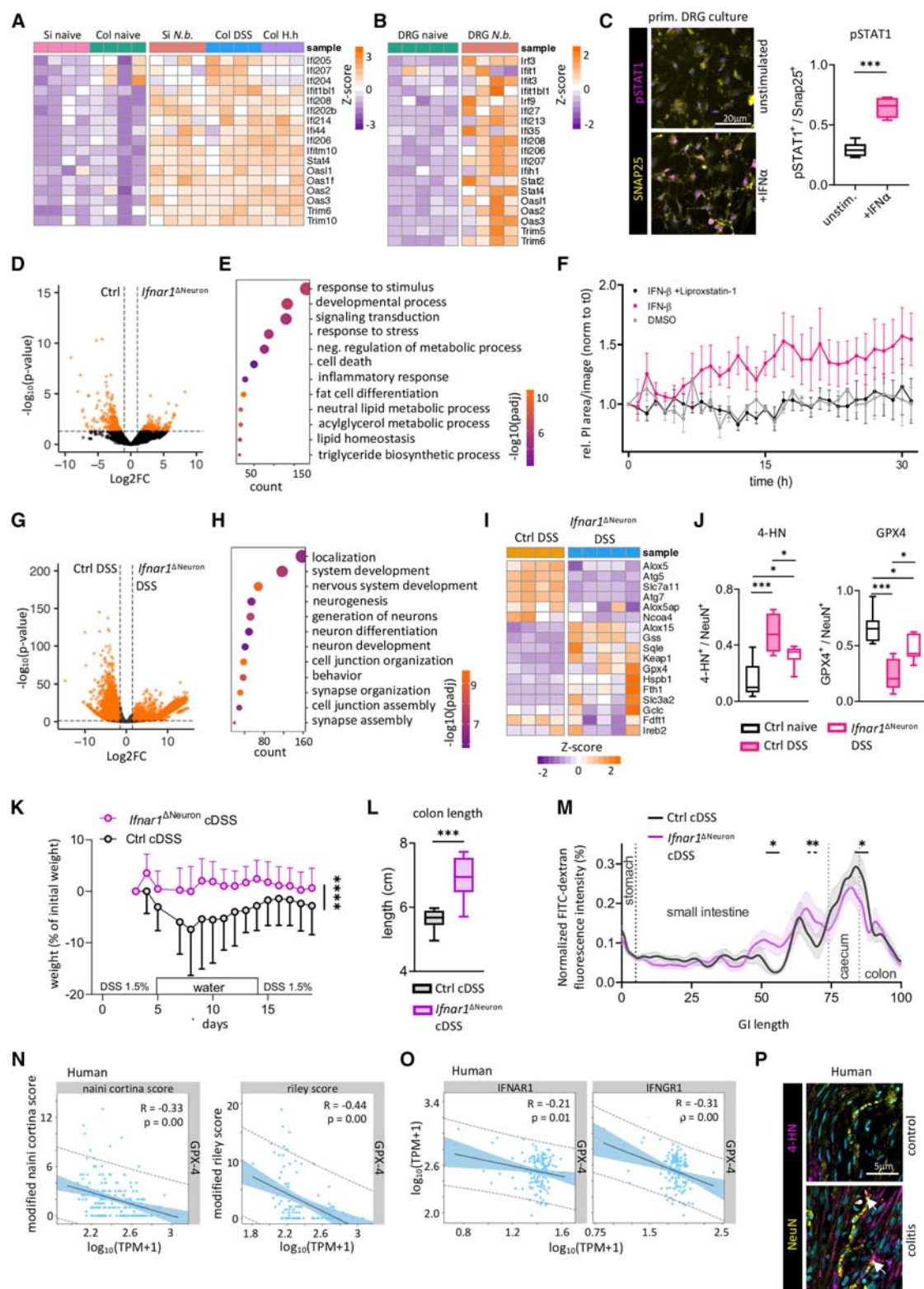
# Neuron
## NeuroResource

- Generic sharing statement: any additional information required to reanalyze the data reported in this study is available from the lead contact upon request.

## CONSORTIA

The members of TRR241 IBDome Consortium are Imke Atreya, Raja Atreya, Petra Bacher, Christoph Becker, Christian Bojarski, Nathalie Britzen-Laurent, Caroline Bosch-Voskens, Hyun-Dong Chang, Andreas Diefenbach, Claudia Günther, Ahmed N. Hegazy, Kai Hildner, Christoph S. N. Klose, Kristina Koop, Susanne Krug, Anja A. Kühl, Moritz Leppkes, Rocío López-Posadas, Leif S.-H. Ludwig, Clemens Neufert, Markus Neurath, Jay V. Patankar, Magdalena Prüß, Andreas Radbruch, Chiara Romagnani, Francesca Ronchi, Ashley Sanders, Alexander Scheffold, Jörg-Dieter Schulzke, Michael Schumann, Sebastian Schürmann, Britta Siegmund, Michael Stürzl, Zlatko Trajanoski, Antigoni Triantafyllopoulou, Maximilian Waldner, Carl Weidinger, Stefan Wirtz, and Sebastian Zundler.

## ACKNOWLEDGMENTS

## AUTHOR CONTRIBUTIONS

P.M.F. and M.O.J. carried out most experiments and analyzed the data. M.B., H.L., Y.L., P.T., L.B., N.S., S.B., A.P., and M.W. helped perform the experiments. C.C. generated visualizations. D.Y., M.G.-A., and R.B. helped with bulk and single-cell RNA-seq analysis. A.A.K., C.W., A.N.H., and J.V.P. provided crucial input and tools for the study. M.O.J. and C.S.N.K. conceived the project and wrote the manuscript with input from all co-authors.

## DECLARATION OF INTERESTS

The authors declare no competing interests.

## DECLARATION OF GENERATIVE AI AND AI-ASSISTED TECHNOLOGIES IN THE WRITING PROCESS

During the preparation of this work, Grammarly was used to correct mistakes. After use, the authors reviewed and edited the content as needed and take full responsibility for the content of the publication.

## STAR★METHODS

Detailed methods are provided in the online version of this paper and include the following:

- KEY RESOURCES TABLE
- EXPERIMENTAL MODELS AND STUDY PARTICIPANTS
  - Mouse strains
  - Disease Models
  - Human Samples
- METHOD DETAILS
  - Tissue Preparation
  - Isolation of Nuclei
  - Sort-purification of nuclei
  - Quantitative real-time PCR
  - Bulk RNA-seq analysis
  - Single nuclei RNA-sequencing and analysis
  - Immunofluorescence microscopy
  - Ferroptosis Assay
  - Gut motility assay using oral FITC-dextran
  - Primary DRG Culture
  - Western Blotting

---

**Figure 7. Neuronal *Ifnar1* signaling regulates ferroptosis, neuronal loss, and gut-transit time**

(A and B) Heatmaps of upregulated interferon pathway-related genes in the ENS and DRGs. Each column in the heatmap represents data from one mouse.

(C) Neuronal DRG culture unstimulated or exposed to IFN-$\alpha$, stained for pSTAT1 (magenta) and SNAP25 (yellow). pSTAT1$^+$ neurons quantified per SNAP25$^+$ neurons ($n = 3$).

(D and G) Volcano plot of dysregulated genes in colonic myenteric neurons of $Snap25^{Cre/+} Ifnar1^{fl/fl} Rosa26^{Sun1-Gfp/+}$ ($Ifnar1^{\Delta Neuron}$) mice compared with Ctrl ($Snap25^{Cre/+} Ifnar1^{+/+} Rosa26^{Sun1-Gfp/+}$) mice in steady state (D) and after DSS-induced colitis (G).

(E and H) GO:BP pathway analysis of dysregulated genes ($p$ adj. $< 0.05$, $1.5 < \log_2 FC < -1.5$), conditions as in (D) and (G) in steady state (E) and after DSS-induced colitis (H).

(F) Ferroptosis assay on neuronal cultures derived from primary colonic myenteric plexus peals stimulated with IFN-$\beta$, IFN-$\beta$, and Liproxstatin-1 or DMSO and monitored for propidium iodide uptake ($n = 3$).

(I) Heatmap showing ferroptosis-related genes in colonic myenteric neurons after DSS-induced colitis of $Ifnar1^{\Delta Neuron}$ mice compared with Ctrl mice (Ctrl DSS $n = 4$, $Ifnar1^{\Delta Neuron}$ DSS $n = 5$).

(J) Quantification of 4-HN$^+$ and GPX4$^+$ colonic myenteric neurons quantified per NeuN$^+$ neurons in Ctrl and $Ifnar1^{\Delta Neuron}$ mice, conditions as indicated. (Ctrl naive $n = 5$, Ctrl DSS $n = 5$, $Ifnar1^{\Delta Neuron}$ DSS $n = 6$.)

(K–M) Chronic DSS-induced colitis (Ctrl $n = 8$, $Ifnar1^{\Delta Neuron}$ $n = 8$). (K) Daily weights compared with the starting weight. (L) Colon length in centimeter (cm). (M) Gut motility assessed by FITC-dextran gavage. FITC distribution was analyzed, and geometric mean fluorescence intensity was calculated.

(N) Negative correlation of *Gpx4* expression and the histopathological scoring systems of Naini and Cortina,[51] as well as the Riley score[52] in patients with inflammatory bowel disease (IBD).

(O) Negative correlation of *Gpx4* with *Ifnar1* or *Ifngr1* expression in the same IBD cohort.

(P) Colonic samples from control (non-affected tissue from control patient; $n = 3$) and colitis patient ($n = 6$) showing 4-HN (magenta), SNAP25 (yellow), and DAPI (blue). Si, small intestine; Col, colon; *N. b.*, *Nippostrongylus brasilienis*; *H. h.*, *Helicobacter hepaticus*; DSS, dextran-sulfate-sodium-induced colitis; DRGs, dorsal root ganglia. Mean ± SD, Student's t test (C and L), one-way ANOVA (J) and two-way ANOVA (F, K, and M). *$p < 0.05$, **$p < 0.01$, ***$p < 0.001$, ****$p < 0.0001$.

- QUANTIFICATION AND STATISTICAL ANALYSIS

## SUPPLEMENTAL INFORMATION

## REFERENCES

1. Veiga-Fernandes, H., and Mucida, D. (2016). Neuro-immune interactions at barrier surfaces. Cell *165*, 801–811. https://doi.org/10.1016/j.cell.2016.04.041.

2. Sharkey, K.A., and Mawe, G.M. (2023). The enteric nervous system. Physiol. Rev. *103*, 1487–1564. https://doi.org/10.1152/physrev.00018.2022.

3. Klose, C.S.N., Mahlakõiv, T., Moeller, J.B., Rankin, L.C., Flamar, A.L., Kabata, H., Monticelli, L.A., Moriyama, S., Putzel, G.G., Rakhilin, N., et al. (2017). The neuropeptide neuromedin U stimulates innate lymphoid cells and type 2 inflammation. Nature *549*, 282–286. https://doi.org/10.1038/nature23676.

4. Cardoso, V., Chesné, J., Ribeiro, H., García-Cassani, B., Carvalho, T., Bouchery, T., Shah, K., Barbosa-Morais, N.L., Harris, N., and Veiga-Fernandes, H. (2017). Neuronal regulation of type 2 innate lymphoid cells via neuromedin U. Nature *549*, 277–281. https://doi.org/10.1038/nature23469.

5. Borovikova, L.V., Ivanova, S., Zhang, M., Yang, H., Botchkina, G.I., Watkins, L.R., Wang, H., Abumrad, N., Eaton, J.W., and Tracey, K.J. (2000). Vagus nerve stimulation attenuates the systemic inflammatory response to endotoxin. Nature *405*, 458–462. https://doi.org/10.1038/35013070.

6. Muller, P.A., Koscsó, B., Rajani, G.M., Stevanovic, K., Berres, M.L., Hashimoto, D., Mortha, A., Leboeuf, M., Li, X.M., Mucida, D., et al. (2014). Crosstalk between muscularis macrophages and enteric neurons regulates gastrointestinal motility. Cell *158*, 300–313. https://doi.org/10.1016/j.cell.2014.04.050.

7. Moriyama, S., Brestoff, J.R., Flamar, A.L., Moeller, J.B., Klose, C.S.N., Rankin, L.C., Yudanin, N.A., Monticelli, L.A., Putzel, G.G., Rodewald, H.R., et al. (2018). beta2-adrenergic receptor-mediated negative regulation of group 2 innate lymphoid cell responses. Science *359*, 1056–1061. https://doi.org/10.1126/science.aan4829.

8. Talbot, J., Hahn, P., Kroehling, L., Nguyen, H., Li, D., and Littman, D.R. (2020). Feeding-dependent VIP neuron-ILC3 circuit regulates the intestinal barrier. Nature *579*, 575–580. https://doi.org/10.1038/s41586-020-2039-9.

9. Seillet, C., Luong, K., Tellier, J., Jacquelot, N., Shen, R.D., Hickey, P., Wimmer, V.C., Whitehead, L., Rogers, K., Smyth, G.K., et al. (2020). The neuropeptide VIP confers anticipatory mucosal immunity by regulating ILC3 activity. Nat Immunol *21*, 168–177. https://doi.org/10.1038/s41590-019-0567-y.

10. Jarret, A., Jackson, R., Duizer, C., Healy, M.E., Zhao, J., Rone, J.M., Bielecki, P., Sefik, E., Roulis, M., Rice, T., et al. (2020). Enteric nervous system-derived IL-18 orchestrates mucosal barrier immunity. Cell *180*, 50–63.e12. https://doi.org/10.1016/j.cell.2019.12.016.

11. Yan, Y., Ramanan, D., Rozenberg, M., McGovern, K., Rastelli, D., Vijaykumar, B., Yaghi, O., Voisin, T., Mosaheb, M., Chiu, I., et al. (2021). Interleukin-6 produced by enteric neurons regulates the number and phenotype of microbe-responsive regulatory T cells in the gut. Immunity *54*, 499–513.e5. https://doi.org/10.1016/j.immuni.2021.02.002.

12. Gonzalez Acera, M., Bubeck, M., Mascia, F., Diemand, L., Sturm, G., Kühl, A.A., Atreya, R., Lie, D.C., Neurath, M.F., Schumann, M., et al. (2021). Dynamic, transient, and robust increase in the innervation of the inflamed mucosa in inflammatory bowel diseases. Cells *10*, 2253. https://doi.org/10.3390/cells10092253.

13. Houser, M.C., and Tansey, M.G. (2017). The gut-brain axis: is intestinal inflammation a silent driver of Parkinson's disease pathogenesis? NPJ Parkinsons Dis. *3*, 3. https://doi.org/10.1038/s41531-016-0002-0.

14. Beatty, J.K., Bhargava, A., and Buret, A.G. (2014). Post-infectious irritable bowel syndrome: mechanistic insights into chronic disturbances following enteric infection. World J. Gastroenterol. *20*, 3976–3985. https://doi.org/10.3748/wjg.v20.i14.3976.

15. Sperber, A.D., Bangdiwala, S.I., Drossman, D.A., Ghoshal, U.C., Simren, M., Tack, J., Whitehead, W.E., Dumitrascu, D.L., Fang, X., Fukudo, S., et al. (2021). Worldwide prevalence and burden of functional gastrointestinal disorders, results of Rome foundation global study. Gastroenterology *160*, 99–114.e3. https://doi.org/10.1053/j.gastro.2020.04.014.

16. Matheis, F., Muller, P.A., Graves, C.L., Gabanyi, I., Kerner, Z.J., Costa-Borges, D., Ahrends, T., Rosenstiel, P., and Mucida, D. (2020). Adrenergic signaling in muscularis macrophages limits infection-induced neuronal loss. Cell *180*, 64–78.e16. https://doi.org/10.1016/j.cell.2019.12.002.

17. Tang, D., Chen, X., Kang, R., and Kroemer, G. (2021). Ferroptosis: molecular mechanisms and health implications. Cell Res. *31*, 107–125. https://doi.org/10.1038/s41422-020-00441-1.

18. Zeisel, A., Hochgerner, H., Lönnerberg, P., Johnsson, A., Memic, F., van der Zwan, J., Häring, M., Braun, E., Borm, L.E., La Manno, G., et al. (2018). Molecular architecture of the mouse nervous system. Cell *174*, 999–1014.e22. https://doi.org/10.1016/j.cell.2018.06.021.

19. Morarach, K., Mikhailova, A., Knoflach, V., Memic, F., Kumar, R., Li, W., Ernfors, P., and Marklund, U. (2021). Diversification of molecularly defined myenteric neuron classes revealed by single-cell RNA sequencing. Nat Neurosci *24*, 34–46. https://doi.org/10.1038/s41593-020-00736-x.

20. Drokhlyansky, E., Smillie, C.S., Van Wittenberghe, N., Ericsson, M., Griffin, G.K., Eraslan, G., Dionne, D., Cuoco, M.S., Goder-Reiser, M.N., Sharova, T., et al. (2020). The human and mouse enteric nervous system at single-cell resolution. Cell *182*, 1606–1622.e23. https://doi.org/10.1016/j.cell.2020.08.003.

21. Wright, C.M., Schneider, S., Smith-Edwards, K.M., Mafra, F., Leembruggen, A.J.L., Gonzalez, M.V., Kothakapa, D.R., Anderson, J.B., Maguire, B.A., Gao, T., et al. (2021). scRNA-seq reveals new enteric nervous system roles for GDNF, NRTN, and TBX3. Cell. Mol. Gastroenterol. Hepatol. *11*, 1548–1592.e1. https://doi.org/10.1016/j.jcmgh.2020.12.014.

22. Mo, A., Mukamel, E.A., Davis, F.P., Luo, C., Henry, G.L., Picard, S., Urich, M.A., Nery, J.R., Sejnowski, T.J., Lister, R., et al. (2015). Epigenomic signatures of neuronal diversity in the mammalian brain. Neuron *86*, 1369–1384. https://doi.org/10.1016/j.neuron.2015.05.018.

23. Harris, J.A., Hirokawa, K.E., Sorensen, S.A., Gu, H., Mills, M., Ng, L.L., Bohn, P., Mortrud, M., Ouellette, B., Kidney, J., et al. (2014). Anatomical characterization of Cre driver mice for neural circuit mapping and manipulation. Front. Neural Circuits *8*, 76. https://doi.org/10.3389/fncir.2014.00076.

24. Gabanyi, I., Muller, P.A., Feighery, L., Oliveira, T.Y., Costa-Pinto, F.A., and Mucida, D. (2016). Neuro-immune interactions drive tissue programming in intestinal macrophages. Cell *164*, 378–391. https://doi.org/10.1016/j.cell.2015.12.023.

25. Jakob, M.O., Kofoed-Branzk, M., Deshpande, D., Murugan, S., and Klose, C.S.N. (2021). An integrated view on neuronal subsets in the peripheral nervous system and their role in immunoregulation. Front. Immunol. *12*, 679055. https://doi.org/10.3389/fimmu.2021.679055.

26. Renthal, W., Tochitsky, I., Yang, L., Cheng, Y.C., Li, E., Kawaguchi, R., Geschwind, D.H., and Woolf, C.J. (2020). Transcriptional reprogramming of distinct peripheral sensory neuron subtypes after axonal injury. Neuron *108*, 128–144.e9. https://doi.org/10.1016/j.neuron.2020.07.026.

27. Wang, K., Wang, S., Chen, Y., Wu, D., Hu, X., Lu, Y., Wang, L., Bao, L., Li, C., and Zhang, X. (2021). Single-cell transcriptomic analysis of somatosensory neurons uncovers temporal development of neuropathic pain. Cell Res. 31, 904–918. https://doi.org/10.1038/s41422-021-00479-9.

28. Muller, P.A., Matheis, F., Schneeberger, M., Kerner, Z., Jové, V., and Mucida, D. (2020). Microbiota-modulated CART(+) enteric neurons autonomously regulate blood glucose. Science 370, 314–321. https://doi.org/10.1126/science.abd6176.

29. Kupari, J., Häring, M., Agirre, E., Castelo-Branco, G., and Ernfors, P. (2019). An atlas of vagal sensory neurons and their molecular specialization. Cell Rep. 27, 2508–2523.e4. https://doi.org/10.1016/j.celrep.2019.04.096.

30. Wallrapp, A., Riesenfeld, S.J., Burkett, P.R., Abdulnour, R.E.E., Nyman, J., Dionne, D., Hofree, M., Cuoco, M.S., Rodman, C., Farouq, D., et al. (2017). The neuropeptide NMU amplifies ILC2-driven allergic lung inflammation. Nature 549, 351–356. https://doi.org/10.1038/nature24029.

31. Matteoli, G., Gomez-Pinilla, P.J., Nemethova, A., Di Giovangiulio, M., Cailotto, C., van Bree, S.H., Michel, K., Tracey, K.J., Schemann, M., Boesmans, W., et al. (2014). A distinct vagal anti-inflammatory pathway modulates intestinal muscularis resident macrophages independent of the spleen. Gut 63, 938–948. https://doi.org/10.1136/gutjnl-2013-304676.

32. Maßberg, D., and Hatt, H. (2018). Human olfactory receptors: novel cellular functions outside of the nose. Physiol. Rev. 98, 1739–1763. https://doi.org/10.1152/physrev.00013.2017.

33. McNab, F., Mayer-Barber, K., Sher, A., Wack, A., and O'Garra, A. (2015). Type I interferons in infectious disease. Nat. Rev. Immunol. 15, 87–103. https://doi.org/10.1038/nri3787.

34. Meseguer, V., Alpizar, Y.A., Luis, E., Tajada, S., Denlinger, B., Fajardo, O., Manenschijn, J.A., Fernández-Peña, C., Talavera, A., Kichko, T., et al. (2014). TRPA1 channels mediate acute neurogenic inflammation and pain produced by bacterial endotoxins. Nat. Commun. 5, 3125. https://doi.org/10.1038/ncomms4125.

35. Pan, Z., Shan, Q., Gu, P., Wang, X.M., Tai, L.W., Sun, M., Luo, X., Sun, L., and Cheung, C.W. (2018). miRNA-23a/CXCR4 regulates neuropathic pain via directly targeting TXNIP/NLRP3 inflammasome axis. J. Neuroinflammation 15, 29. https://doi.org/10.1186/s12974-018-1073-0.

36. Leung, L., and Cahill, C.M. (2010). TNF-alpha and neuropathic pain–a review. J. Neuroinflammation 7, 27. https://doi.org/10.1186/1742-2094-7-27.

37. Cook, A.D., Christensen, A.D., Tewari, D., McMahon, S.B., and Hamilton, J.A. (2018). Immune cytokines and their receptors in inflammatory pain. Trends Immunol. 39, 240–255. https://doi.org/10.1016/j.it.2017.12.003.

38. Zhang, C., Hu, M.W., Wang, X.W., Cui, X., Liu, J., Huang, Q., Cao, X., Zhou, F.Q., Qian, J., He, S.Q., et al. (2022). scRNA-sequencing reveals subtype-specific transcriptomic perturbations in DRG neurons of Pirt(EGFPf) mice in neuropathic pain condition. eLife 11, e76063. https://doi.org/10.7554/eLife.76063.

39. Hockley, J.R.F., Taylor, T.S., Callejo, G., Wilbrey, A.L., Gutteridge, A., Bach, K., Winchester, W.J., Bulmer, D.C., McMurray, G., and Smith, E.S.J. (2019). Single-cell RNAseq reveals seven classes of colonic sensory neuron. Gut 68, 633–644. https://doi.org/10.1136/gutjnl-2017-315631.

40. Ekblad, E., Edvinsson, L., Wahlestedt, C., Uddman, R., Håkanson, R., and Sundler, F. (1984). Neuropeptide Y co-exists and co-operates with noradrenaline in perivascular nerve fibers. Regul. Pept. 8, 225–235. https://doi.org/10.1016/0167-0115(84)90064-8.

41. Lundberg, J.M., Rudehill, A., Sollevi, A., Fried, G., and Wallin, G. (1989). Co-release of neuropeptide Y and noradrenaline from pig spleen in vivo: importance of subcellular storage, nerve impulse frequency and pattern, feedback regulation and resupply by axonal transport. Neuroscience 28, 475–486. https://doi.org/10.1016/0306-4522(89)90193-0.

42. Pang, X.Y., Wang, S., Jurczak, M.J., Shulman, G.I., and Moise, A.R. (2017). Retinol saturase modulates lipid metabolism and the production of reactive oxygen species. Arch. Biochem. Biophys. 633, 93–102. https://doi.org/10.1016/j.abb.2017.09.009.

43. Kagan, V.E., Mao, G., Qu, F., Angeli, J.P.F., Doll, S., Croix, C.S., Dar, H.H., Liu, B., Tyurin, V.A., Ritov, V.B., et al. (2017). Oxidized arachidonic and adrenic PEs navigate cells to ferroptosis. Nat. Chem. Biol. 13, 81–90. https://doi.org/10.1038/nchembio.2238.

44. Beatty, A., Singh, T., Tyurina, Y.Y., Tyurin, V.A., Samovich, S., Nicolas, E., Maslar, K., Zhou, Y., Cai, K.Q., Tan, Y., et al. (2021). Ferroptotic cell death triggered by conjugated linolenic acids is mediated by ACSL1. Nat. Commun. 12, 2244. https://doi.org/10.1038/s41467-021-22471-y.

45. Guerrero-Hue, M., García-Caballero, C., Palomino-Antolín, A., Rubio-Navarro, A., Vázquez-Carballo, C., Herencia, C., Martín-Sanchez, D., Farré-Alins, V., Egea, J., Cannata, P., et al. (2019). Curcumin reduces renal damage associated with rhabdomyolysis by decreasing ferroptosis-mediated cell death. FASEB J. 33, 8961–8975. https://doi.org/10.1096/fj.201900077R.

46. Linkermann, A., Chen, G., Dong, G., Kunzendorf, U., Krautwald, S., and Dong, Z. (2014). Regulated cell death in AKI. J. Am. Soc. Nephrol. 25, 2689–2701. https://doi.org/10.1681/ASN.2014030262.

47. Lee, J.Y., Nam, M., Son, H.Y., Hyun, K., Jang, S.Y., Kim, J.W., Kim, M.W., Jung, Y., Jang, E., Yoon, S.J., et al. (2020). Polyunsaturated fatty acid biosynthesis pathway determines ferroptosis sensitivity in gastric cancer. Proc. Natl. Acad. Sci. USA 117, 32433–32442. https://doi.org/10.1073/pnas.2006828117.

48. Marchetti, M., Monier, M.N., Fradagrada, A., Mitchell, K., Baychelier, F., Eid, P., Johannes, L., and Lamaze, C. (2006). Stat-mediated signaling induced by type I and type II interferons (IFNs) is differentially controlled through lipid microdomain association and clathrin-dependent endocytosis of IFN receptors. Mol. Biol. Cell 17, 2896–2909. https://doi.org/10.1091/mbc.e06-01-0076.

49. Kalie, E., Jaitin, D.A., Podoplelova, Y., Piehler, J., and Schreiber, G. (2008). The stability of the ternary interferon-receptor complex rather than the affinity to the individual subunits dictates differential biological activities. J. Biol. Chem. 283, 32925–32936. https://doi.org/10.1074/jbc.M806019200.

50. Chen, W., Teo, J.M.N., Yau, S.W., Wong, M.Y.M., Lok, C.N., Che, C.M., Javed, A., Huang, Y., Ma, S., and Ling, G.S. (2022). Chronic type I interferon signaling promotes lipid-peroxidation-driven terminal CD8(+) T cell exhaustion and curtails anti-PD-1 efficacy. Cell Rep. 41, 111647. https://doi.org/10.1016/j.celrep.2022.111647.

51. Naini, B.V., and Cortina, G. (2012). A histopathologic scoring system as a tool for standardized reporting of chronic (ileo)colitis and independent risk assessment for inflammatory bowel disease. Hum. Pathol. 43, 2187–2196. https://doi.org/10.1016/j.humpath.2012.03.008.

52. Riley, S.A., Mani, V., Goodman, M.J., Dutt, S., and Herd, M.E. (1991). Microscopic activity in ulcerative colitis: what does it mean? Gut 32, 174–178. https://doi.org/10.1136/gut.32.2.174.

53. Xu, M., Tao, J., Yang, Y., Tan, S., Liu, H., Jiang, J., Zheng, F., and Wu, B. (2020). Ferroptosis involves in intestinal epithelial cell death in ulcerative colitis. Cell Death Dis. 11, 86. https://doi.org/10.1038/s41419-020-2299-1.

54. Foster, S.L., Seehus, C.R., Woolf, C.J., and Talbot, S. (2017). Sense and immunity: context-dependent neuro-immune interplay. Front. Immunol. 8, 1463. https://doi.org/10.3389/fimmu.2017.01463.

55. Lazear, H.M., Schoggins, J.W., and Diamond, M.S. (2019). Shared and distinct functions of type I and Type III interferons. Immunity 50, 907–923. https://doi.org/10.1016/j.immuni.2019.03.025.

56. Chhatbar, C., Detje, C.N., Grabski, E., Borst, K., Spanier, J., Ghita, L., Elliott, D.A., Jordão, M.J.C., Mueller, N., Sutton, J., et al. (2018). Type I interferon receptor signaling of neurons and astrocytes regulates microglia activation during viral encephalitis. Cell Rep. 25, 118–129.e4. https://doi.org/10.1016/j.celrep.2018.09.003.

57. Chotiwan, N., Rosendal, E., Willekens, S.M.A., Schexnaydre, E., Nilsson, E., Lindqvist, R., Hahn, M., Mihai, I.S., Morini, F., Zhang, J., et al. (2023). Type I interferon shapes brain distribution and tropism of tick-borne Flavivirus. Nat. Commun. *14*, 2007. https://doi.org/10.1038/s41467-023-37698-0.

58. Roy, E.R., Chiu, G., Li, S., Propson, N.E., Kanchi, R., Wang, B., Coarfa, C., Zheng, H., and Cao, W. (2022). Concerted type I interferon signaling in microglia and neural cells promotes memory impairment associated with amyloid beta plaques. Immunity *55*, 879–894.e6. https://doi.org/10.1016/j.immuni.2022.03.018.

59. Hosseini, S., Michaelsen-Preusse, K., Grigoryan, G., Chhatbar, C., Kalinke, U., and Korte, M. (2020). Type I interferon receptor signaling in astrocytes regulates hippocampal synaptic plasticity and cognitive function of the healthy CNS. Cell Rep. *31*, 107666. https://doi.org/10.1016/j.celrep.2020.107666.

60. Donnelly, C.R., Jiang, C., Andriessen, A.S., Wang, K., Wang, Z., Ding, H., Zhao, J., Luo, X., Lee, M.S., Lei, Y.L., et al. (2021). STING controls nociception via type I interferon signalling in sensory neurons. Nature *591*, 275–280. https://doi.org/10.1038/s41586-020-03151-1.

61. ElTanbouly, M.A., and Noelle, R.J. (2021). Rethinking peripheral T cell tolerance: checkpoints across a T cell's journey. Nat. Rev. Immunol. *21*, 257–267. https://doi.org/10.1038/s41577-020-00454-2.

62. Dejas, L., Santoni, K., Meunier, E., and Lamkanfi, M. (2023). Regulated cell death in neutrophils: from apoptosis to NETosis and pyroptosis. Semin. Immunol. *70*, 101849. https://doi.org/10.1016/j.smim.2023.101849.

63. Ye, L., Li, G., Goebel, A., Raju, A.V., Kong, F., Lv, Y., Li, K., Zhu, Y., Raja, S., He, P., et al. (2020). Caspase-11-mediated enteric neuronal pyroptosis underlies Western diet-induced colonic dysmotility. J. Clin. Invest. *130*, 3621–3636. https://doi.org/10.1172/JCI130176.

64. Ahrends, T., Aydin, B., Matheis, F., Classon, C.H., Marchildon, F., Furtado, G.C., Lira, S.A., and Mucida, D. (2021). Enteric pathogens induce tissue tolerance and prevent neuronal loss from subsequent infections. Cell *184*, 5715–5727.e12. https://doi.org/10.1016/j.cell.2021.10.004.

65. Ocansey, D.K.W., Yuan, J., Wei, Z., Mao, F., and Zhang, Z. (2023). Role of ferroptosis in the pathogenesis and as a therapeutic target of inflammatory bowel disease (Review). Int. J. Mol. Med. *51*, 53. https://doi.org/10.3892/ijmm.2023.5256.

66. Ou, M., Jiang, Y., Ji, Y., Zhou, Q., Du, Z., Zhu, H., and Zhou, Z. (2022). Role and mechanism of ferroptosis in neurological diseases. Mol. Metab. *61*, 101502. https://doi.org/10.1016/j.molmet.2022.101502.

67. Dehghani, T., Gholizadeh, O., Daneshvar, M., Nemati, M.M., Akbarzadeh, S., Amini, P., Afkhami, H., Kohansal, M., Javanmard, Z., and Poortahmasebi, V. (2023). Association between inflammatory bowel disease and viral infections. Curr. Microbiol. *80*, 195. https://doi.org/10.1007/s00284-023-03305-0.

68. Canavan, C., West, J., and Card, T. (2014). The epidemiology of irritable bowel syndrome. Clin. Epidemiol. *6*, 71–80. https://doi.org/10.2147/CLEP.S40245.

69. Wadi, W.F., Rathi, M.H., and Molan, A.L. (2021). The possible link between intestinal parasites and irritable bowel syndrome (IBS) in Diyala Province, Iraq. Ann. Parasitol. *67*, 505–513. https://doi.org/10.17420/ap6703.364.

70. Dieleman, L.A., Palmen, M.J., Akol, H., Bloemena, E., Peña, A.S., Meuwissen, S.G., and Van Rees, E.P. (1998). Chronic experimental colitis induced by dextran sulphate sodium (DSS) is characterized by Th1 and Th2 cytokines. Clin. Exp. Immunol. *114*, 385–391. https://doi.org/10.1046/j.1365-2249.1998.00728.x.

71. Yang, X.O., Chang, S.H., Park, H., Nurieva, R., Shah, B., Acero, L., Wang, Y.H., Schluns, K.S., Broaddus, R.R., Zhu, Z., et al. (2008). Regulation of inflammatory responses by IL-17F. J. Exp. Med. *205*, 1063–1075. https://doi.org/10.1084/jem.20071978.

72. Yang, W.L., Qiu, W., Zhang, T., Xu, K., Gu, Z.J., Zhou, Y., Xu, H.J., Yang, Z.Z., Shen, B., Zhao, Y.L., et al. (2023). Nsun2 coupling with RoRgammat

73. shapes the fate of Th17 cells and promotes colitis. Nat. Commun. *14*, 863. https://doi.org/10.1038/s41467-023-36595-w.

73. West, N.R., Hegazy, A.N., Owens, B.M.J., Bullers, S.J., Linggi, B., Buonocore, S., Coccia, M., Görtz, D., This, S., Stockenhuber, K., et al. (2017). Oncostatin M drives intestinal inflammation and predicts response to tumor necrosis factor-neutralizing therapy in patients with inflammatory bowel disease. Nat. Med. *23*, 579–589. https://doi.org/10.1038/nm.4307.

74. Ryzhakov, G., West, N.R., Franchini, F., Clare, S., Ilott, N.E., Sansom, S.N., Bullers, S.J., Pearson, C., Costain, A., Vaughan-Jackson, A., et al. (2018). Alpha kinase 1 controls intestinal inflammation by suppressing the IL-12/Th1 axis. Nat. Commun. *9*, 3797. https://doi.org/10.1038/s41467-018-06085-5.

75. Xu, M., Pokrovskii, M., Ding, Y., Yi, R., Au, C., Harrison, O.J., Galan, C., Belkaid, Y., Bonneau, R., and Littman, D.R. (2018). c-MAF-dependent regulatory T cells mediate immunological tolerance to a gut pathobiont. Nature *554*, 373–377. https://doi.org/10.1038/nature25500.

76. Kamphuis, E., Junt, T., Waibler, Z., Forster, R., and Kalinke, U. (2006). Type I interferons directly regulate lymphocyte recirculation and cause transient blood lymphopenia. Blood *108*, 3253–3261. https://doi.org/10.1182/blood-2006-06-027599.

77. Chassaing, B., Aitken, J.D., Malleshappa, M., and Vijay-Kumar, M. (2014). Dextran sulfate sodium (DSS)-induced colitis in mice. Curr. Protoc. Immunol. *104*, 15.25.11–15.25.14. https://doi.org/10.1002/0471142735.im1525s104.

78. Schiering, C., Krausgruber, T., Chomka, A., Fröhlich, A., Adelmann, K., Wohlfert, E.A., Pott, J., Griseri, T., Bollrath, J., Hegazy, A.N., et al. (2014). The alarmin IL-33 promotes regulatory T-cell function in the intestine. Nature *513*, 564–568. https://doi.org/10.1038/nature13577.

79. Kullberg, M.C., Jankovic, D., Feng, C.G., Hue, S., Gorelick, P.L., McKenzie, B.S., Cua, D.J., Powrie, F., Cheever, A.W., Maloy, K.J., et al. (2006). IL-23 plays a key role in Helicobacter hepaticus-induced T cell-dependent colitis. J. Exp. Med. *203*, 2485–2494. https://doi.org/10.1084/jem.20061082.

80. Erkert, L., Gamez-Belmonte, R., Kabisch, M., Schödel, L., Patankar, J.V., Gonzalez-Acera, M., Mahapatro, M., Bao, L.L., Plattner, C., Kühl, A.A., et al. (2024). Alzheimer's disease-related presenilins are key to intestinal epithelial cell function and gut immune homoeostasis. Gut *73*, 1618–1631. https://doi.org/10.1136/gutjnl-2023-331622.

81. Häring, M., Fatt, M., and Kupari, J. (2020). Protocol to prepare single-cell suspensions from mouse vagal sensory ganglia for transcriptomic studies. Star Protoc. *1*, 100030. https://doi.org/10.1016/j.xpro.2020.100030.

82. Sleigh, J.N., Weir, G.A., and Schiavo, G. (2016). A simple, step-by-step dissection protocol for the rapid isolation of mouse dorsal root ganglia. BMC Res. Notes *9*, 82. https://doi.org/10.1186/s13104-016-1915-8.

83. Muller, P.A., Schneeberger, M., Matheis, F., Wang, P., Kerner, Z., Ilanges, A., Pellegrino, K., Del Mármol, J., Castro, T.B.R., Furuichi, M., et al. (2020). Microbiota modulate sympathetic neurons via a gut-brain circuit. Nature *583*, 441–446. https://doi.org/10.1038/s41586-020-2474-7.

84. Dobin, A., Davis, C.A., Schlesinger, F., Drenkow, J., Zaleski, C., Jha, S., Batut, P., Chaisson, M., and Gingeras, T.R. (2013). STAR: ultrafast universal RNA-seq aligner. Bioinformatics *29*, 15–21. https://doi.org/10.1093/bioinformatics/bts635.

85. Liao, Y., Smyth, G.K., and Shi, W. (2014). featureCounts: an efficient general purpose program for assigning sequence reads to genomic features. Bioinformatics *30*, 923–930. https://doi.org/10.1093/bioinformatics/btt656.

86. Love, M.I., Huber, W., and Anders, S. (2014). Moderated estimation of fold change and dispersion for RNA-seq data with DESeq2. Genome Biol. *15*, 550. https://doi.org/10.1186/s13059-014-0550-8.

87. Szklarczyk, D., Kirsch, R., Koutrouli, M., Nastou, K., Mehryary, F., Hachilif, R., Gable, A.L., Fang, T., Doncheva, N.T., Pyysalo, S., et al. (2023). The STRING database in 2023: protein-protein association networks and

functional enrichment analyses for any sequenced genome of interest. Nucleic Acids Res. *51*, D638–D646. https://doi.org/10.1093/nar/gkac1000.

88. Milacic, M., Beavers, D., Conley, P., Gong, C., Gillespie, M., Griss, J., Haw, R., Jassal, B., Matthews, L., May, B., et al. (2024). The Reactome pathway knowledgebase 2024. Nucleic Acids Res. *52*, D672–D678. https://doi.org/10.1093/nar/gkad1025.

89. Martens, M., Ammar, A., Riutta, A., Waagmeester, A., Slenter, D.N., Hanspers, K., A Miller, R., Digles, D., Lopes, E.N., Ehrhart, F., et al. (2021). WikiPathways: connecting communities. Nucleic Acids Res. *49*, D613–D621. https://doi.org/10.1093/nar/gkaa1024.

90. Kanehisa, M., and Goto, S. (2000). KEGG: kyoto encyclopedia of genes and genomes. Nucleic Acids Res. *28*, 27–30. https://doi.org/10.1093/nar/28.1.27.

91. Thomas, P.D., Ebert, D., Muruganujan, A., Mushayahama, T., Albou, L.P., and Mi, H. (2022). PANTHER: making genome-scale phylogenetics accessible to all. Protein Sci. *31*, 8–22. https://doi.org/10.1002/pro.4218.

92. Hao, Y., Stuart, T., Kowalski, M.H., Choudhary, S., Hoffman, P., Hartman, A., Srivastava, A., Molla, G., Madad, S., Fernandez-Granda, C., et al. (2024). Dictionary learning for integrative, multimodal and scalable single-cell analysis. Nat. Biotechnol. *42*, 293–304. https://doi.org/10.1038/s41587-023-01767-y.

93. Hao, Y., Hao, S., Andersen-Nissen, E., Mauck, W.M., 3rd, Zheng, S., Butler, A., Lee, M.J., Wilk, A.J., Darby, C., Zager, M., et al. (2021). Integrated analysis of multimodal single-cell data. Cell *184*, 3573–3587.e29. https://doi.org/10.1016/j.cell.2021.04.048.

94. Stuart, T., Butler, A., Hoffman, P., Hafemeister, C., Papalexi, E., Mauck, W.M., 3rd, Hao, Y., Stoeckius, M., Smibert, P., and Satija, R. (2019). Comprehensive integration of single-cell data. Cell *177*, 1888–1902.e21. https://doi.org/10.1016/j.cell.2019.05.031.

95. Schneider, R., Leven, P., Mallesh, S., Breßer, M., Schneider, L., Mazzotta, E., Fadda, P., Glowka, T., Vilz, T.O., Lingohr, P., et al. (2022). IL-1-dependent enteric gliosis guides intestinal inflammation and dysmotility and modulates macrophage function. Commun. Biol. *5*, 811. https://doi.org/10.1038/s42003-022-03772-4.

96. Laddach, A., Chng, S.H., Lasrado, R., Progatzky, F., Shapiro, M., Erickson, A., Sampedro Castaneda, M., Artemov, A.V., Bon-Frauches, A.C., Amaniti, E.M., et al. (2023). A branching model of lineage differentiation underpinning the neurogenic potential of enteric glia. Nat. Commun. *14*, 5904. https://doi.org/10.1038/s41467-023-41492-3.

97. Koester, S.T., Li, N., Lachance, D.M., and Dey, N. (2021). Marker-based assays for studying gut transit in gnotobiotic and conventional mouse models. Star Protoc. *2*, 100938. https://doi.org/10.1016/j.xpro.2021.100938.

**CellPress**
OPEN ACCESS

**Neuron**
**NeuroResource**

# STAR★METHODS

## KEY RESOURCES TABLE

| REAGENT or RESOURCE | SOURCE | IDENTIFIER |
|---|---|---|
| **Antibodies** | | |
| Anti-mouse: mouse anti-SNAP-25 Antibody (SMI 81) | BioLegend | Cat# 129804; RRID: AB_2564674 |
| Anti-mouse: mouse anti-beta-3 Tubulin (2G10-TB3) | Invitrogen | Cat# 14-4510-82 |
| Anti-mouse: rabbit anti-HuC/HuD | Abcam | Cat# ab210554 |
| Anti-mouse: rabbit anti-HuD + HuC AF488 | Abcam | Cat# ab237234 |
| Anti-mouse: mouse anti-NeuN (A60) | Sigma-Aldrich | Cat# MAB377 |
| Anti-mouse: anti-IFNAR1 (MAR1-5A3) | BioLegend | Cat# 127302 RRID: AB_1089153 |
| Anti-mouse: rat anti-IL33R (ST2) (U29-93) | BD | Cat# 566311 RRID: AB_2744490 |
| Anti-mouse: rabbit anti-4 Hydroxynonenal | Abcam | Cat# ab46545 |
| Anti-mouse: rabbit anti-GPX4 (EPNCIR144) | Abcam | Cat# ab125066 |
| Anti-mouse: rabbit anti-OLFR56 | Thermo Scientific | Cat# OSR00031G |
| Anti-mouse: rabbit anti-TRPM8 (M571) | Novus Biologicals | Cat# NBP1-97311SS |
| Anti-mouse: rabbit anti-TRPV1 (VR1) | Novus Biologicals | Cat# NB100-1617 |
| Anti-mouse IL-23R-APC (12B2B64) | BioLegend | Cat# 150905; RRID: AB_2687345 |
| Anti-mouse: polyclonal affinity purified IgG goat anti-Sox10 | Provided by Prof. Michael Wegner, Erlangen | N/A |
| Anti-mouse: mouse anti-TUBB3 (TUJ1) | BioLegend | Cat# 801213 RRID: AB_2313773 |
| Anti-mouse: rabbit anti-TLR4 (MTS510) | BioLegend | Cat# 117601; RRID: AB_313788 |
| Anti-mouse: rabbit anti-phospho STAT1 | Cell Signaling | Cat# 9167S |
| β-Actin (13E5) Rabbit anti-mouse | Cell Signaling | Cat# #4970 |
| IL-10R-blocking antibody | BioXCell | Cat# CD210 |
| Anti-rabbit: IgG (H+L) goat, Alexa Fluor® 488 | Thermo Fischer Scientific | Cat# A11008 |
| Anti-rabbit: donkey Alexa Fluor® 555 | BioLegend | Cat# 406412 |
| Anti-rabbit: donkey Alexa Fluor® 555 | Thermo Fischer Scientific | Cat# A31572 |
| Anti-mouse: IgG1 goat, Alexa Fluor® 488 | Thermo Fischer Scientific | Cat# A21121 |
| Anti-mouse: IgG goat Alexa Fluor® 555 | BioLegend | Cat# 405324 |
| Anti-goat: IgG donkey Alexa Fluor® 647 | Invitrogen | Cat# A21447 |
| Anti-Rat: IgG (H+L) Goat Secondary Antibody, Alexa Fluor® 594 | Invitrogen | Cat# A-11007 |
| Anti-mouse CD127-PE/Cy7 | Biolegend | Cat# 135014; RRID: AB_1937265 |
| Anti-mouse KLRG1-Alexa Fluor 647 | eBioscience | Cat# 51-5893-82; RRID: AB_2744744 |
| Anti-mouse CD45-BUV395 | BD | Cat# 564279; RRID: AB_2651134 |
| Anti-mouse CD3e-PerCP-Cyanine5.5 | Thermo Fischer Scientific | Cat# 45-0031-82; RRID: AB_906226 |
| Anti-mouse CD5-PerCP-Cyanine5.5 | Thermo Fischer Scientific | Cat# 45-0051-82; RRID: AB_914334 |
| Anti-mouse FceR1alpha- PerCP-eFluor 710 | Thermo Fischer Scientific | Cat# 46-5898-82; RRID: AB_2573801 |
| Anti-mouse Ly6G- PerCP-eFluor 710 | Thermo Fischer Scientific | Cat# 46-9668-82; RRID: AB_2573893 |
| Anti-mouse CD19-PerCP-Cyanine5.5 | Thermo Fischer Scientific | Cat# 45-0193-82; RRID: AB_906215 |
| Sytox Blue Dead Cell Stain | Thermo Scientific | Cat# S34857 |
| **Biological samples** | | |
| 6 colon samples from ulcerative colitis | IBDome | N/A |
| 3 control samples from cancer resections, non-inflamed | IBDome | N/A |
| **Chemicals, Peptides, and Recombinant Proteins** | | |
| Formaldehydlösung 4% neutral | SAV Liquid Production GmbH | Cat# FN-5000-4-1 |
| Paraformaldehyd granuliert | Carl Roth | Cat# 0335.1 |

*(Continued on next page)*

## Neuron
### NeuroResource

***Continued***

| REAGENT or RESOURCE | SOURCE | IDENTIFIER |
|---|---|---|
| Dulbeccos PBS (w/o calcium and magnesium) (DPBS) | Gibco | Cat# 4190-094 |
| Dulbeccos PBS (w calcium and magnesium) (PBS) | Gibco | Cat# D8662 |
| Trizol | Thermo Fisher Scientific | Cat# 15596026 |
| HEPES (1 M) | Gibco | Cat# 15630080 |
| KCL | Merck | Cat# P3911 |
| MgCl2 | Sigma-Aldrich | Cat# 1374248 |
| Fetal bovine serum | Pan-Biotech | Cat# P30-3602 |
| Bovine Serum Albumin | Fisher Scientific | Cat# FERB14 |
| Chloroform | Sigma Aldrich | Cat# 288306-100ML |
| 70 kD Fluorescein isothiovyanate (FITC)-dextran | Sigma | Cat# 46945-100MG |
| Sakura Finetek™ Tissue-Tek™ O.C.T. Compound | Sakura | Cat# 12351753 |
| SuperFrost® Plus | VWR | Cat# 631-9483 |
| Tris | Merck | Cat# T1503 |
| Triton X-100 | Sigma-Aldrich | Cat# X100-100ML |
| Tween | Serva | Cat#39796.01 |
| Heparin | Sigma-Aldrich | Cat# H3393-250KU |
| Saponin | Merck | Cat# 84510 |
| Saccharose | Sigma-Aldrich | Cat# S9378-500G |
| DTT | AppliChem | Cat# A3668,0050 |
| PIC | Fisher Scientific | Cat# BDB554724 |
| Superase inhibitor | Thermo Fisher | Cat# AM2696 |
| Fluoromount-G | Invitrogen | Cat# 00-4958-02 |
| Mouse Serum | Life Science | Cat# S-012L |
| DAPI (4',6-Diamidino-2-Phenylindole, Dilactate) | BioLegend | Cat# 422801 |
| Propidium iodide | ThermoFisher | Cat# R37108 |
| Normal Donkey Serum | Merck | Cat# S30-100ML |
| Goat Serum | Jackson ImmunoResearch | Cat# 005-000-121 |
| Dextran sulfate sodium powder | MP Biomedical | Cat# 0216011080 |
| Collagenase type II | Merck | Cat# C2-22 |
| Collagenase D | Roche | Cat# 11088866001 |
| TrypLE express Enzyme | ThermoFisher | Cat# 12604013 |
| F12 medium | ThermoFisher | Cat# 15172529 |
| Penicillin-streptomycin | ThermoFisher | Cat# 11548876 |
| Primocin | InvivoGen | Cat# ant-pm-05 |
| Neurobasal A | ThermoFisher | Cat# 10888022 |
| B-27 supplement | ThermoFisher | Cat# 17504044 |
| GlutaMAX supplement | ThermoFisher | Cat# 35050061 |
| Matrigel growth factor | Corning | Cat# 356231 |
| Arachidonic acid | Sigma Aldrich | Cat# A3611 |
| RSL3 | Selleckchem | Cat# S8155 |
| Erastin | Selleckchem | Cat# S7242 |
| Liproxstatin-1 | Selleckchem | Cat# S7699 |
| IFN-ß | Biotechne | Cat# 8234-MB-010 |
| IFN-γ | Immunotools GmbH | Cat# 12343536 |
| Poly-L-Ornithine | Sigma-Aldrich | Cat# P4957 |
| Laminin | Sigma-Aldrich | Cat# L6274 |
| Trypsin-EDTA | Sigma-Aldrich | Cat# T4049 |
| Arac | Sigma-Aldrich | Cat# C6645 |

(*Continued on next page*)

*Continued*

| REAGENT or RESOURCE | SOURCE | IDENTIFIER |
|---|---|---|
| **Critical Commercial Assays** | | |
| miRNeasy Micro Kit | Qiagen | Cat# 217084 |
| In Situ Cell Death Detection Kit, TMR red | Sigma-Aldrich | Cat# 12156792910 |
| SMARTer Stranded Total RNA-Seq Kit – Pico | Takara | Cat# 634485 |
| High-Capacity cDNA Reverse Transcription Kit | Thermo Fisher | Cat# 4374966 |
| SYBR™ Green PCR Master Mix | Thermo Fisher | Cat# 4367659 |
| Taqman™ Universal Master Mix | Applied Biosystems | Cat# 4448510 |
| **Deposited Data** | | |
| Raw sequencing data from bulk and single-nucleus RNA-seq (fastq files) | European Nucleotide Archive | https://www.ebi.ac.uk/ena/browser/view/PRJEB75453; Accession number: PRJEB75453 |
| Human IBDome cohort (v0.50) transcriptomic data | IBDome | https://ibdome.org. |
| Bulk RNA-seq of ENS, DRG, SMG, VG of steady state vs inflammation (web-based screening of data; raw data: RNA-seq count data used for the analyses; processed data: normalized count data) | Github | https://dyusuf.github.io/Transcriptional_Atlas_GI_Neurons_Inflammation/ |
| Dataset and analysis code used for RNA-seq analysis | Zenodo | https://doi.org/10.5281/zenodo.14879230 |
| Tool used to generate the protein cluster data | Zenodo | https://doi.org/10.5281/zenodo.14879657 |
| **Experimental Models: Organisms/Strains (all Mus musculus)** | | |
| C57BL/6J (wild-type) | Janvier | N/A |
| Snap25[cre/+] | Jackson | JAX strain #023525 |
| INTACT^{fl/fl} | Jackson | JAX strain #021039 |
| Ifnar1^{fl/fl} | Ulrich Kalinke, Kamphuis et al.[76]; PMID: 16868248 | N/A |
| **Oligonucleotides** | | |
| See Table S1 for Oligonucleotides and RNA sequences | | |
| **Software and Algorithms** | | |
| FlowJo10.4 | FlowJo, LLC, OR, USA | https://www.flowjo.com/solutions/flowjo; RRID:SCR_008520 |
| GraphPad Prism V8 | GraphPad Software, San Diego, USA | https://www.graphpad.com/scientific-software/prism/; RRID:SCR_002798 |
| ImageJ 1.8.0 | National Institutes of Health, USA | https://imagej.nih.gov/ij/ |
| Adobe Photoshop | Adobe | https://creativecloud.adobe.com/apps/download/photoshop |
| R studio 2024.09.0+375 | R foundation | https://www.r-project.org; RRID:SCR_000432 |
| Seurat 5.1.0 | Satija Lab, New York Genome Center, USA | https://satijalab.org/seurat/ |

## EXPERIMENTAL MODELS AND STUDY PARTICIPANTS

### Mouse strains

C57BL/6 mice were purchased from Janvier. *Snap25*[cre/+] (JAX strain #023525, B6;129S-*Snap25*[tm2.1(cre)Hze]/J),[23] INTACT mice (JAX strain #021039, B6;129-*Gt(ROSA)26Sor*[tm5(CAG-Sun1/sfGFP)Nat]/J),[22] and *Ifnar1*[fl/fl][76] on a C57BL/6 background were bred locally at Charité. Sex and age-matched animals were used for experiments if not otherwise indicated. We did not observe differences between sexes in all experimental settings. We did not use randomization to assign animals to experimental groups. All animal experiments were approved and are in accordance with the local animal care committees (Landesamt für Gesundheit und

# Neuron
## NeuroResource

**CellPress**
OPEN ACCESS

## Disease Models
### Acute DSS-induced colitis
2.5% Dextran sulfate sodium powder (MP Biomedical Order Nr. 0216011080) was added to the drinking water for consecutive 5 days.[77] Mice were monitored twice a day and onset of the disease was verified by histology. Day 7 after disease induction, mice were euthanized and tissues were collected for further analysis.

### Chronic DSS-colitis
1.5% Dextran sulfate sodium was added to the drinking water for 5 consecutive days. Thereafter mice were allowed to recover for 9 days. Another cycle of 1.5% DSS was applied and mice were harvested 20 days later.

### Helminth infection
Third-stage larvae (L3) of *N. brasiliensis* were purified with a Baermann apparatus. After washing three times in PBS, larvae were counted and 500 purified larvae were injected subcutaneously in PBS. Mice were killed and organs were analyzed 7 days post infection.

### Helicobacter hepaticus + α-IL-10R colitis
Experimental colitis was induced as previously described.[78,79] Briefly, mice were fed $1 \times 10^8$ colony-forming units (c.f.u.) of *H. hepaticus* by oral gavage delivered with a 22G curved blunted needle on days 0 and 1 of the experiment. 1 mg of an IL-10R-blocking antibody (clone 1B1.2) was administered as an intraperitoneal injection once weekly starting at day 0. In this model, disease severity peaks between 14 and 21 d after disease induction.

## Human Samples
Transcriptomic data of the IBDome cohort used for the correlations is publicly available.[80] Written informed consent was obtained from all patients All experiments involving human material were approved by the institutional review board of the Charité-Universitätsmedizin Berlin (EA1_200_17).

Inflamed colon specimens were obtained from ulcerative colitis patients, which underwent surgical colectomy due to colitis [6 Patients, 3 female (19-52y), 3 male (24-53y)], while control specimens were obtained from non-affected, non-inflamed tissue of tumor resection [3 male patients (24-77)]. 1-2 μm sections were cut from formalin-fixed and paraffin-embedded tissues.

## METHOD DETAILS

### Tissue Preparation
Mice were killed by cervical dislocation and the small intestine or colon was removed, cleaned from remaining fat tissue and washed in ice-cold phosphate buffered saline (PBS). Tissues were cut open longitudinally and washed in ice cold PBS to remove intestinal contents and mucus. For dissection of the muscularis, the intestinal tissue was placed on a chilled plate with the serosa facing up.[24,76] Curved forceps were used to carefully scrape off the muscularis sheet. The vagal ganglia, the superior mesenteric ganglion and the DRGs were dissected under a stereo microscope (Zeiss Stereo Discovery v.20) according to previously published protocols.[81–83] The obtained DRG were either collected in 0.3% collagenase (Sigma-Aldrich) for primary DRG cultures, in cold PBS for immunoflourescence staining or snap frozen in liquid nitrogen for Western Blotting.

### Isolation of Nuclei
The following method for nuclei extractions was performed for mouse small intestinal muscularis, colon muscularis, DRG, SMG or VG. For isolation of nuclei from the small intestine and the colon, fresh-frozen tissues were disaggregated in 2 mL of custom nuclear extraction buffer NIM2 (NIM1 (250 mM Sucrose, 25 mM KCl, 5 mM $MgCl_2$, 10 mM Tris Buffer pH=8), 1 μM dithiothreitol (DTT), protease inhibitor cocktail (PIC) (1:100), Superase Inhibitor (1:100), 0,1% Triton X-100) with mild chopping by Fine Scissors for 10 minutes on ice.[20] Large debris were removed with a 40 μm strainer (Falcon). An additional 0,5 mL of buffer was used to wash the filter before proceeding to fluorescence-activated cell sorting (FACS). Nuclei were then pelleted at 500g for 5 mins at 4°C. Supernatant was discarded and the nuclei pellet was resuspended in 250 μL of NIM2 buffer after the addition of DAPI. For isolation of nuclei from the VG, the SMG and DRGs, dounce homogenization using a 2 mL Dounce Tissue Grinder combined with chopping was performed. The buffers and tissue handling remained equivalent as for the ENS.

### Sort-purification of nuclei
Nuclei were stained with DAPI (Biolegend) in NIM2 buffer. Fluorescence-activating sort purification was performed on a custom configuration FACSAria cell sorter (BD Biosciences). Single nuclei (DAPI+, GFP+) were purified and validated under the microscope for integrity prior to RNA isolation. Samples were stored at −80°C until whole-transcriptome amplification, library construction, sequencing, and processing.

## Quantitative real-time PCR

Sorted nuclei were homogenized in Trizol (Thermo Fisher Scientific) and stored at -80°C. RNA was extracted with chloroform. Reverse transcription of total RNA was performed using the High Capacity cDNA Reverse Transcription kit according to the protocol provided by the manufacturer (Thermo Fisher Scientific). Reaction was detected on a QuantStudio 5 Real-Time PCR (Thermo Fisher Scientific) using the Power SYBR Green Master Mix (Thermo Fisher Scientific) or the Taqman Gene Expression Assays (Applied Biosystems). The following Taqman Assays were used: *Snap25* (Mm01276449_m1), *Nmu* (Mm00479868_m1), *Vip* (Mm00660234_m1), *Chat* (Mm01221882_m1). Gene expression was normalized to the housekeeping gene *Hprt1* (Mm00446968_m1).

## Bulk RNA-seq analysis

Neuronal nuclei were sort-purified (DAPI$^+$, GFP$^+$) from the small intestine, colon, DRG, VG or SMG of 8 weeks old, littermate, male *Snap25*$^{Cre/+}$ INTACT (*Rosa26*$^{Sun1-Gfp/+}$) or *Snap25*$^{Cre/+}$ *Ifnar1*$^{fl/fl}$ INTACT mice as indicated. Nuclei were sorted into Trizol (Thermo Fisher Scientific) and RNA was isolated using the microRNeasy Plus Micro kit (Qiagen) according to the protocol provided by the manufacturer. RNA-seq libraries were prepared by the MDC BIMSB Core Bioinformatic Facility using the SMARTer Stranded Total RNA-Seq Kit – Pico (Takara). Sequencing was performed on a NovaSeq 6000 (Illumina), yielding 100 bp single-end reads. RNA-Seq reads were mapped to the mouse genome (mm10) with STAR[84] version 2.7.11a using default parameters. Reads were assigned to genes with FeatureCounts[85] with the following parameters: -t exon -g gene_id, gene annotation was performed on GRCm38(mm10). The differential expression was carried out with DESeq2 version 1.22.1[86] using default parameters. The protein network construction, along with subsequent cluster detection and functional enrichment analyses, were conducted using an in-house tool developed by D.Y. and R.B. The protein associations were retrieved from the String database,[87] with a cutoff association score of 0.7. To identify functionally related protein groups, we employed the Louvain modularity algorithm for cluster detection. To identify overrepresented functions within the protein clusters, we performed hypergeometric testing against gene sets curated from four pathway databases.[88–91] This analysis employed a FDR cutoff of 0.05 to ensure statistically significant results.

## Single nuclei RNA-sequencing and analysis

Nuclei were sort-purified as described above from 8 week-old male mice for all conditions into landing buffer containing 0.1% BSA and RNAse inhibitor. Nuclei were validated for integrity under the microscope. Single nuclei RNA-seq libraries were generated according to the Chromium Next GEM Single Cell 3' Reagent Kits v3.1 User Guide (CG000204) by 10xGenomics. Briefly, a droplet emulsion was generated in a microfluidic chip followed by barcoded cDNA generation inside the droplets. Purified and amplified cDNA was then subjected to library preparation, and sequenced on aNovaSeq 6000 instrument (Illumina) to a minimal depth of 40000 mean reads per cell. Raw sequence reads were processed using cellranger (version 5.0.0), including the default detection of intact cells. Mkfastq and count were used in default parameter settings for demultiplexing and quantification of gene expression. Refdata-cellranger-mm10-1.2.0 was used as reference. Single-nucleus RNA-seq data alignment and gene expression quantification was carried out with Cellranger (version-5.0.0), using as a reference refdata-gex-mm10-2020-A mouse genome. Cellranger outpur was analyzed with R (version 4.3.0) using the Seurat package (version 4.9.9). All analyses were performed using a filtered feature barcode matrix. We excluded genes expressed in less than 3 cells and cells expressing less than 200 genes or more than 2500 (VG) genes or 5000 (DRG, SMG) genes, as well as cells with more than 5% mitochondrial reads.

Counts were normalized and scaled using SCTransform and SclaeData. Dimensionality reduction was done using RunPCA and variable features were identified with VariableFeatures. FindNeighbours and FindClusters functions were used with resolutions ranging from 0.1-0.3 to identify clusters. Signature genes were identified using FindAllMarkers in default parameter settings. Two Seurat objects were integrated using FindIntegrationAnchors, IntegrateData, FindVariableGenes, RunPCA, RunUMAP, FindNeighbours and FindClusters functions. UMAPs and violin plots were performed on normalized data using SCT as DefaultAssay.[92–94]

## Immunofluorescence microscopy

For whole mount staining, the tissue from 8-12 week old age-and sex-matched male or female mice was fixed in 4% PFA and kept in PBS at 4°C and until staining.[83] Briefly, whole mount samples were first permeabilized for 2 h at RT in PTxwH (0.5% Triton X-100/ 0.05% Tween-20/4 μg heparin). Samples were then blocked for 2 h at RT in blocking buffer (PTxwH with 5% BSA, 5% donkey and 5% goat serum). Antibodies were added to the blocking buffer at and incubated for 2 days at 4°C with shaking. After primary incubation the tissue was washed four times in PTxwH and incubated in blocking buffer with secondary antibodies for 2 h at RT. Samples were again washed four times in PTxwH and then mounted.

For cryo-sections, the tissue was fixed in 4% PFA, dehydrated in sucrose at 4°C overnight, embedded in OCT and stored at -20°C. Sections were cut at 10 μm and collected onto SuperfrostPlus slides. The sections were fixed in acetone at -20°C, incubated with 50mM glycine for antigen retrieval and permeabilized in 0.5% saponin. Blocking was performed with PBS-T (PBS and 0.5% Triton X-100) and 10% donkey serum and stained.

The following antibodies were used: mouse anti SNAP25 (SMI81), mouse anti- TUBB3 (TUJ1), mouse anti-IFNAR1 (MAR1-5A3), mouse anti-IL23R (12B2B64), rabbit anti-TUBB3 (2G10-TB3), rabbit anti-OLFR56 (MOR276-1), rabbit anti-4-HN (ab46545), rabbit anti-TRPV1 (VR1), rabbit anti-TRPM8 (M571), rabbit anti-Il33R (RMST2-33), rabbit anti-TLR4 (MTS510), followed by donkey anti-rabbit or goat-anti mouse antibody coupled to Alexa Fluor 488 or 555 (Thermo Fisher Scientific) and nuclei were counterstained with

DAPI (Thermo Fisher Scientific). TUNEL (TdT-mediated dUTP-biotin nick end labeling) staining was performed using the In Situ Cell Death Detection Kit, TMR red (Roche) according to the manual. Images were captured under a Zeiss Axio Observer 7 microscope and analysed with Zen software (Zeiss). For quantitative analysis of electron micrographs, images were processed using ImageJ.

## Ferroptosis Assay

The culturing of enteric neuroglia from the longitudinal muscle myenteric plexus peels was performed as previously reported with some modifications.[95,96] Briefly, after killing the mice the small intestines were dissected and divided into three equal parts and flushed with ice cold PBS. The peels were rinsed thrice with ice cold PBS centrifuging each time for 30 seconds at 400 x g. After the last rinse, add 5 ml digestion medium consisting of 1.3 mg ml$^{-1}$ Collagenase type II (Merck, Cat. No. C2-22), 10% FCS (Sigma-Aldrich, Cat. No. F7524), made in PSB and mince peels with scissors. The peels were digested at 37°C, for 60 minutes with gentle vortexing every 10 minutes. After the digestion, cells were collected by centrifugation for 7 min at 400 x g at 4°C. The supernatant was discarded and the pellet was resuspended in 2.5ml of room temperature TrypLE express Enzyme (ThermoFisher, Cat. No. 12604013) and digested further for 5 minutes in a shaking water bath at 37°C. The digestion enzymes were neutralized with 5 mL of cold rinse media consisting of 1X F12 medium (ThermoFisher, Cat. No. 15172529) supplemented with 10% FCS (Sigma-Aldrich, Cat. No. F7524), 1% penicillin-streptomycin (ThermoFisher, Cat. No. 11548876), and 100 μg ml$^{-1}$ Primocin (InvivoGen, Cat. No. ant-pm-05). The cells were strained through a 70μm sterile disposable cell strainer centrifuged and resuspended in complete neuronal medium (CNM) consisting of Neurobasal A (ThermoFisher, Cat. No. 10888022), supplemented with 1X B-27 supplement (ThermoFisher, Cat. No. 17504044), and 1mM L-alanyl-L-glutamine (GlutaMAX supplement, ThermoFisher, Cat. No. 35050061) and triturated using 1ml tips or glass polished pasture pipettes. The cells were passed through a 70μm cell strainer, centrifuged, and resuspended in complete neuronal medium and seeded into cell culture plates coated with Matrigel growth factor reduced (diluted 1:30) (Corning, 356231) and cultured at 37°C with 5% CO2 with medium replacement every 2 days. After seven days, cells were seeded onto optically compatible Matrigel coated tissue culture plates in CNM using TrzpLE. The cells were allowed 1 day of recovery before treatment and acquisition of propidium iodide (ThermoFisher, Cat. No., R37108) signal using the IncuCyte system (Sartorius). The cells were treated with the indicated concentrations and in combinations as indicated with the following compounds: Arachidonic acid (Sigma Aldrich, Cat. No. A3611), GPX4 inhibitor RSL3 (Selleckchem, Cat. No. S8155), system Xc− inhibitor Erastin (Selleckchem, Cat. No. S7242), Liproxstatin-1 (Selleckchem, Cat. No. S7699), IFN-ß (Biotechne, Cat. No. 8234-MB-010), IFN-γ (Immunotools GmbH, Cat. No. 12343536).

## Gut motility assay using oral FITC-dextran

Mice were given 200μL of a 3.75mg/mL FITC-dextran (average mol wt. 4,000, Merck GmbH) solution prepared in Lipofundin MCT 20% (Braun GmbH) by oral gavage. After 4h, mice were killed by cervical dislocation and whole GI tracts were isolated and placed in ice-cold PBS to inhibit residual motility. Next, the distribution of the FITC dextran within the GI tract was analyzed by acquiring fluorescence images using the Amersham Image Quant 800 system. For quantification, the fluorescence intensity along the GI tract was measured using ImageJ2 by outlining the GI tract and applying the "Plot profile" command. This measurement was performed thrice and the resulting intensity profiles were averaged, smoothed and the x-axis converted from length in pixels to length in percent. Lastly, fluorescence intensity values were normalized to the total fluorescence intensity in the whole GI tract to account for loss of signal intensity due to intestinal barrier defects or leakage after dissection. To compare gut motility between groups, the geometric mean of the FITC-dextran fluorescence intensity was calculated as described in Koester et al.[97] as well as intensity profiles compared using two-way ANOVA.

## Primary DRG Culture

For primary DRG culture, sterile glass cover slips were positioned in 12-well cell culture plates (Greiner Bio-One). First coated with 1 μg/ml Poly-L-Ornithine (Sigma-Aldrich) and then with 25 μg/ml Laminin (Sigma-Aldrich) at 37°C in the incubator for at least 1 hour respectively. Harvested DRGs were collected in 0.3% collagenase (Sigma-Aldrich) and incubated on a shaker at 37°C and 800rpm for 30 minutes to break up the tissue. After centrifugation at 0.3g and 4°C, 5 min, the supernatant was removed. 0.05% Trypsin-EDTA (Sigma-Aldrich) was added to the pellet and incubated on a shaker at 37°C and 800rpm for 30 min. The remaining tissue pellet was disrupted and centrifuged at 0.3g and 4°C for 5 min. Trypsin was removed and the pellet resuspended in medium (150 μl/well) (DMEM/F-12, 10% Horse Serum, 1% Pen/Strep, 1% NEAA, 1% L-Glut, 5μg/mL NGF). The resuspended mixture was then seeded onto the pre-coated cover slips and incubated at 37°C for 10 min. The rest of the medium (350 μl/well) was added. The cells were placed in an incubator at 37°C, 92% humidity and 5% CO2 henceforth. 24 hours after, medium containing 10μM AraC (Sigma-Aldrich) was added to provoke cell cycle arrest in all non-neuronal cells. This was removed after 24 hours and henceforth media were changed every 48h to provide nutrients to the cells. On day 3, when indicated, DRG cultures were stimulated with 40 ng/mL IFN-α overnight, washed and fixed for 5 min with 4% PFA and left in PBS until staining with pSTAT1 and SNAP25.

## Western Blotting

The protein lysate was obtained through manual grinding with a douncer (Millipore Sigma). RIPA buffer (50 mM Tric-Cl (pH8), 1% NP40, 0.5% Na-deoxycholate, 150 mM NaCl, 0.1 mM DTT with Protease Inhibitor Cocktail (Sigma-Aldrich) and Phosphatase

**CellPress**
OPEN ACCESS

**Neuron**
**NeuroResource**

Inhibitor (Thermo Fisher) was added to the lysate and incubated on ice for 1 hour. The lysate was centrifuged at 4°C and 14.000 rpm for 30 minutes. The supernatant was used to quantify the protein in a Bradford assay.

For Immunoblotting, pre-cast 12% SDS-PAGE gels were used (BioRad). Gel and separation was performed using electrophoresis. A Trans-Blot Turbo Transfer System (BioRad) was used to transfer the proteins onto a nitrocellulose membrane (GE Healthcare) at 25V for 23 minutes. The membrane was blocked for 1 hour with 5% milk powder solution in PBS +0.05% Tween-20 (Serva). Antibodies were added to 2% milk powder solution in PBS + 0.05% Tween-20 in an appropriate concentration and incubated for 60 minutes RT and 4°C overnight on the blot. Blot was washed with PBS + 0.05% Tween-20 secondary HRP-conjugated antibody in 2% milk powder and PBS + 0.05% Tween-20 solution was added and incubated for 90 minutes at RT. After washing with PBS + 0.05% Tween-20, the blot was developed using the ECL Kit (Cytiva) and was made visible using a ChemiDoc (BioRad). The blot was analysed by densitometry via ImageJ.

## QUANTIFICATION AND STATISTICAL ANALYSIS

Data is plotted showing the mean +/- standard deviation. P values of data sets were determined by unpaired two-tailed Student's t-test or ordinary one-way ANOVA with Tukey's multiple comparisons test, with 95% confidence interval. All statistical tests were performed with Graph Pad Prism V9 software (GraphPad Software, Inc.). (*$p < 0.05$; **$p < 0.01$; ***$p < 0.001$; ****$p < 0.0001$ and n.s., not significant). Investigators were not blinded to group allocation during experiments. Exact values of n representing number of mice can be found in the figure legends.